ARTICLE

Check for updates

African biomass burning affects aerosol cycling over the Amazon

Bruna A. Holanda [1,2,12], Marco A. Franco [1,2], David Walter [1,3,13], Paulo Artaxo [2], Samara Carbone[4], Yafang Cheng [1], Sourangsu Chowdhury[5,14], Florian Ditas [1,12], Martin Gysel-Beer [6], Thomas Klimach[1], Leslie A. Kremper[1], Ovid O. Krüger [1], Jost V. Lavric [3,15], Jos Lelieveld [5], Chaoqun Ma [1], Luiz A. T. Machado [1,2], Robin L. Modini [6], Fernando G. Morais [2], Andrea Pozzer [5], Jorge Saturno[7,16], Hang Su [1], Manfred Wendisch [8], Stefan Wolff[1], Mira L. Pöhlker[1,8,9], Meinrat O. Andreae [7,10,11], Ulrich Pöschl[1] & Christopher Pöhlker [1,7 ✉]

Smoke from vegetation fires affects air quality, atmospheric cycling, and the climate in the Amazon rain forest. A major unknown has remained the quantity of long-range transported smoke from Africa in relation to local and regional fire emissions. Here we quantify the abundance, seasonality, and properties of African smoke in central Amazonia. We show that it accounts for ~ 60% of the black carbon concentrations during the wet season and ~ 30% during the dry season. The African smoke influences aerosol-radiation interactions across the entire Amazon, with the strongest impact on the vulnerable eastern basin, a hot spot of climate and land use change. Our findings further suggest that the direct influence of African smoke has been historically relevant for soil fertilization, the carbon and water cycles, and, thus, the development of the Amazon forest ecosystem, even in the pre-industrial era.

[1] Multiphase Chemistry Department, Max Planck Institute for Chemistry, 55128 Mainz, Germany. [2] Institute of Physics, University of São Paulo, São Paulo 05508-900, Brazil. [3] Department of Biogeochemical Processes, Max Planck Institute for Biogeochemistry, 07701 Jena, Germany. [4] Institute of Agrarian Sciences, Federal University of Uberlândia, Uberlândia-MG 38408-100, Brazil. [5] Atmospheric Chemistry Department, Max Planck Institute for Chemistry, 55128 Mainz, Germany. [6] Laboratory of Atmospheric Chemistry, Paul Scherrer Institute, 5232 Villigen, PSI, Switzerland. [7] Biogeochemistry Department, Max Planck Institute for Chemistry, 55128 Mainz, Germany. [8] Leipzig Institute for Meteorology, Leipzig University, 04103 Leipzig, Germany. [9] Atmosp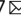heric Microphysics Department, Leibniz Institute for Tropospheric Research, 04318 Leipzig, Germany. [10] Scripps Institution of Oceanography, University of California San Diego, La Jolla, CA 92037, USA. [11] Department of Geology and Geophysics, King Saud University, Riyadh 145111, Saudi Arabia. [12] Present address: Hessian Agency for Nature Conservation, Environment and Geology, 65203 Wiesbaden, Germany. [13] Present address: Climate Geochemistry Department, Max Planck Institute for Chemistry, 55128 Mainz, Germany. [14] Present address: CICERO Center for International Climate Research, 0349 Oslo, Norway. [15] Present address: Acoem Australasia (Ecotech Pty Ltd), 1492 Ferntree Gully Road, Knoxfield VIC, 3180 Melbourne, VIC, Australia. [16] Present address: Physikalisch-Technische Bundesanstalt, 38116 Braunschweig, Germany. ✉email: c.pohlker@mpic.de

Human use of fire in the Amazon has been documented as far back as pre-Columbian times[1]. With the inauguration of the Transamazon Highway in 1970, however, the modern era of deforestation began, and the number of fires reached unprecedented levels[2]. After 2004, a steady decline in deforestation rates and burning activity gave rise to hopes of an end to this development (Supplementary Figs. 1 and 2). Since 2014, however, we have witnessed a trend reversal with again rising deforestation and associated biomass burning across the basin[3]. Emblematic for this development and the heavy smoke covering the Amazon basin in the burning season each year is the 'black rain' event in August 2019 in São Paulo city, 2500 km away from the fires[4].

Biomass burning has been the tool of choice for land clearing and management in agricultural expansion, infrastructure development, and mining in the Amazon[5]. The emitted smoke comprises organic and inorganic aerosol particles, black carbon (BC), as well as various noxious gases[6]. Under smoky conditions, the concentrations of aerosol particles and cloud condensation nuclei (CCN) in the Amazon exceed the natural background by up to two orders of magnitude[7-9]. The smoke alters the Earth's radiative energy budget through absorption and scattering of solar radiation, which leads, for instance, to a surface cooling and a corresponding heating of BC-enriched atmospheric layers above. This can cause a stabilization of the boundary layer up to an inhibition of shallow convective cloud formation[10]. The smoke also affects cloud and precipitation formation and, thus, the (re) cycling of water between biosphere and atmosphere[11-14]. This includes, for instance a delay of the precipitation onset in the clouds to higher altitudes, a corresponding suppression of low-level rainout, as well as an invigoration of the updrafts in deep convective clouds[15,16]. Because of its major atmospheric significance, the properties and roles of biomass burning smoke in the Amazon have been investigated intensely[17-19].

This picture becomes even more complicated by the fact that the Amazonian atmosphere is not only influenced by fires in the Amazon forest and nearby biomes, but also to a large degree by the transatlantic transport of smoke, dust, and other emissions from Africa[20-23]. The African continent is one of the strongest aerosol sources worldwide and the Amazon is located 'downwind' in the Atlantic trade wind circulation[24]. Figure 1a shows the spatiotemporal patterns of African aerosol and other pollutants transport into the Amazon: From December to April, northeasterly air masses transport Saharan dust and smoke from African fires north of the equator towards the Amazon[21,25,26]. From August to November, southeasterly air masses transport smoke from African fires south of the equator towards the Amazon[27-30]. Since the African smoke influx appears to be the rule, rather than the exception, the pollution over the Amazon can be seen as a mixture from South American and African sources with a high spatiotemporal variability. This raises the following fundamental questions:

1. What are the respective contributions and seasonality of South American and African biomass burning smoke to the aerosol burden in Amazonia?
2. How does smoke from the two continents differ in terms of microphysical, chemical, and optical properties and how does this relate to climate-relevant processes, such as the atmospheric radiative energy transfer?
3. Is the transatlantic transport and the influx of African smoke into Amazonia correctly represented in global aerosol models?

Here, we present a technique for the quantitative smoke source apportionment based on the microphysical properties of refractory black carbon (rBC)[31], which refers to carbonaceous particles that are insoluble and vaporize at temperatures near 4000 K emitting a laser-induced incandescence signal[32]. We utilize extensive field data of rBC mass size distributions collected with single particle soot photometers (SP2) deployed over two full seasonal cycles at the Amazon Tall Tower Observatory (ATTO)[33] and on the aircraft missions ACRIDICON-CHUVA over the Amazon[18] and CAFE-Africa over the tropical Atlantic Ocean[34] (Fig. 1b). The observational rBC data are combined with complementary aerosol measurements and global modelling to answer the above questions.

Results and discussion

Some types of aerosol particles originating from distant sources, such as mineral dust and marine aerosols, have characteristic physicochemical properties that facilitate their identification within the Amazonian aerosol population (refs. [25,35]). A distinction between the African biomass burning smoke after transatlantic transport and the regional Amazonian smoke, however, is more challenging. To discriminate between these two sources, we analyzed the rBC microphysical properties at the ATTO site from January 2019 to December 2020 (Supplementary Fig. 3). Based on a detailed analysis of the main wind field, fire counts, and backward trajectories, as shown in Fig. 2, we selected a number of event periods when the dominant influence of either regional or long-range-transported smoke from Africa (or the mixture of both) is expected to arrive at ATTO (more details in Supplementary Note 1.1). We found robust differences in the rBC core size distributions for these event periods that allow to clearly discriminate the influence of African and South American smoke in the Amazon. This refers in particular to the geometric mean diameter (D_{rBC}) and geometric standard deviation (σ_{rBC}) of the rBC mass size distributions. Overall, the data from ATTO consistently shows that the mass size distributions of African rBC cores are narrower and centered at larger diameters than the mass size distributions of the South American rBC cores (Fig. 1c). Specifically, we found average values of $D_{rBC,Afr} = 217 \pm 2$ nm (mean ± one standard deviation) and $\sigma_{rBC,Afr} = 1.48 \pm 0.01$ for the African rBC cores, in contrast to $D_{rBC,SAm} = 181 \pm 3$ nm and $\sigma_{rBC,SAm} = 1.67 \pm 0.02$ for the South American rBC cores during selected event periods at ATTO, with either preponderant African (Afr) or South American (SAm) smoke influence.

The rBC mass size distributions measured at ATTO are remarkably consistent with the aircraft observations (Fig. 1d) at the relevant locations in Fig. 1b: (i) During ACRIDICON-CHUVA, fresh biomass burning plumes were probed directly over Amazonian fires, as a reference case for pure and fresh Amazonian smoke, yielding $D_{rBC,AC,SAm} = 180 \pm 8$ nm and $\sigma_{rBC,AC,SAm} = 1.59 \pm 0.03$. (ii) During the same campaign, we also investigated aged African pollution layers after at least 10 days of transatlantic transport in the free troposphere off the Brazilian coast and prior to being mixed into the Amazonian convective boundary layer[30]. In these layers, we obtained $D_{rBC,AC,Afr} = 202 \pm 8$ nm and $\sigma_{rBC,AC,Af} = 1.49 \pm 0.04$. (iii) During CAFE-Africa, the transatlantic transport of African smoke was targeted at different locations over the Atlantic Ocean and, therefore, at different aging states. Across all of these measurements over the ocean we obtained $D_{rBC,CA,Afr} = 226 \pm 8$ nm and $\sigma_{rBC,CA,Afr} = 1.49 \pm 0.04$. These results indicate that the rBC core properties are conserved during horizontal transport, i.e., the smoke did not undergo relevant cloud processing or coagulational growth that could influence the rBC size distributions[36-38]. Even for the long-range-transported smoke, we do not observe significant changes in rBC core properties from the different locations where African BB was sampled over the Atlantic (Fig. 1 and Supplementary Fig. 4). In fact, while other organic and inorganic aerosols as well
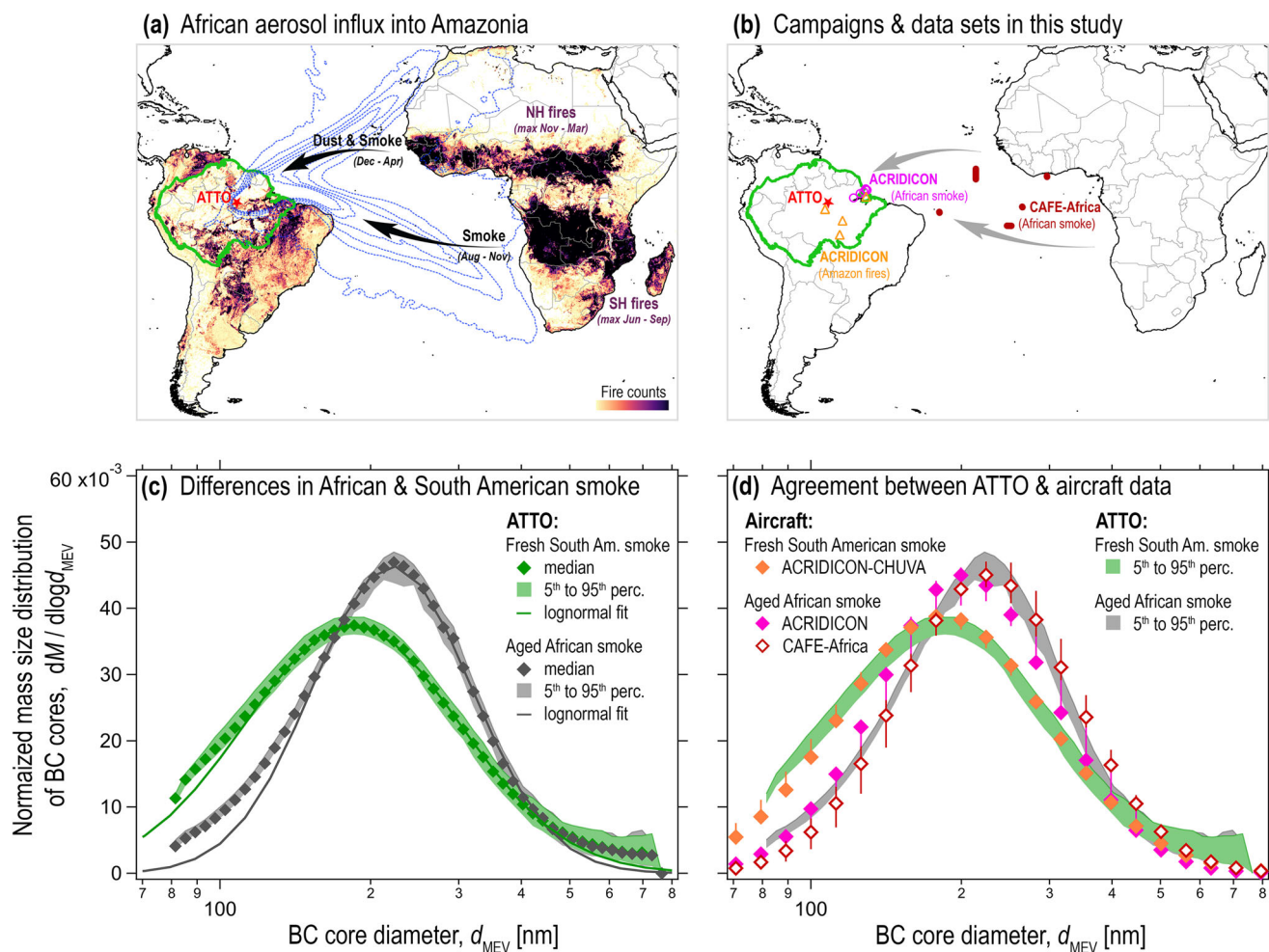
Fig. 1 African smoke transport and characteristic black carbon mass size distributions. a Geography of African biomass burning smoke transport across the Atlantic into the Amazon, **b** locations of ground-based and aircraft measurements analyzed in this study, and **c, d** characteristic differences in the shape of refractory black carbon (rBC) mass size distributions of African vs South American smoke. In (**a**), the Atlantic trade winds north and south of the intertropical conversion zone are shown by means of a backward trajectory ensemble (2011-2020, HYSPLIT model, 10 days) starting at 200 m above ground at ATTO. The fire map represents the average density of fires detected by the satellites Aqua and Terra from 2011 to 2020. In (**b**), the relevant locations include ATTO[33] as well as several flight segments in heavy biomass burning smoke during the aircraft missions ACRIDICON-CHUVA in Sep 2014[18] and CAFE-Africa in Aug and Sep 2018[34]. In (**c**), the rBC mass size distributions as a function of rBC core mass equivalent diameter (d_{MEV}) during event periods under predominant African (20 - 23 Jan and 03 - 09 Feb 2020) vs predominant South American (28 Jul - 11 Aug 2020) smoke influence at ATTO are compared. In (**d**), the ATTO rBC mass size distributions from (**c**) (gray and green shadings) are shown in combination with the aircraft rBC mass size distributions (symbols) for the flight segments in (**b**). The rBC mass size distributions were normalized to the area under the curves. Solid lines are the median, and shadings are the range between the 5th and 95th percentiles of 3 h (ATTO) and 10 seconds averages (aircraft). For statistics and further information refer to Supplementary Fig. 4.

as the BC mixing state remain highly dynamic throughout the smoke life cycle[39,40], the rBC core, as a chemically inert species, remains conserved, at least from the regions where it was measured with the aircraft up to the ATTO site.

These distinctly different rBC signatures make it possible to deconvolute the superposition of the African and South American influences through a bimodal lognormal fit of two years of measured rBC mass size distributions at ATTO. The fit parameters $D_{rBC,i}$ and $\sigma_{rBC,i}$ of one African (Afr) and one South American (SAm) mode were constrained according to the experimental results in Fig. 1c, d, while the rBC mass concentration of each mode ($A_{rBC,i}$) was a free parameter. Examples of individual bimodal fits are shown in Supplementary Fig. 5. The integration of each mode provided the African ($M_{rBC,Afr}$) and South American ($M_{rBC,SAm}$) contributions to the total rBC mass concentration (M_{rBC}) (see Section "Biomass burning aerosol source assignment using the SP2"). The resulting time series of

the rBC mass fractions and absolute mass concentrations attributed to African and South American fires at ATTO are shown in Fig. 3a, b, respectively. In principle, the number of modes (n) fitted to the rBC mass size distributions can be also larger than two, if further combustion sources emit rBC with another microphysical signature distinct enough to be resolved by the multimodal fit. The present analysis is based on a bimodal fit, assuming that biomass burning in Africa and in South America are the two main sources providing BC particles to the ATTO site. This implies that urban pollution – for example from Manaus city[41] – does not play a significant role for the BC properties at ATTO. In fact, the ATTO site was chosen to preclude any significant influence from Manaus, and other major cities are either not covered by the backward trajectory footprint or very far away[24]. A systematic backward trajectory analysis shows that southwesterly winds, which cover the Manaus sector and could potentially transport urban pollution to ATTO,
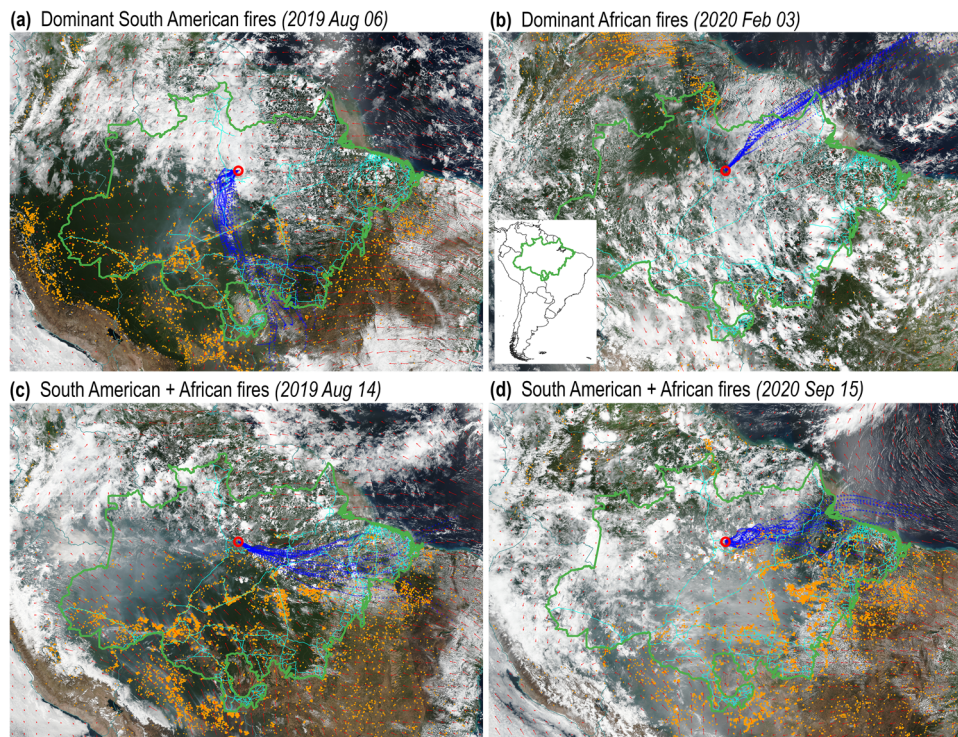
Fig. 2 Amazon Tall Tower Observatory in central Amazonia under different smoke conditions. a Southerly winds transporting smoke from deforestation fires during the period of intense burning on 06 August 2019; **b** Strong easterly winds transporting African biomass burning to the otherwise clean Amazonian conditions on 03 February 2020 during the wet season; **c, d** Dry season days receiving smoke from both, South American and African fires. The figure shows composite maps of satellite images with cloud cover and smoke plumes, individual detected fires (yellow dots), overall wind fields at 950 hPa (red arrows), and HYSPLIT 3 d backward trajectory (BT) ensembles (blue dots) started at the ATTO site (red circular markers). The green boundary shows the legal Amazon region. Light blue lines show the major highways in the Amazon basin. Details on the creation of the maps can be found in the method sections on backward trajectories and geographic information system (GIS) data and processing.

accounts for only 1.4 % of the trajectories during an eight years period[24]. This suggests that urban influence from Manaus at ATTO represents a rather exceptional case. Further, previous studies showed that urban rBC is characterized by even smaller rBC core sizes[42,43]. That means that, if present, urban rBC would show up as a third mode at diameters smaller than the South American rBC peak. As the monomodal lognormal distributions in Supplementary Fig. 3c, d show no shoulder or distortion towards smaller core diameters, we have no indications to assume that a major urban influence was present. If present in diluted amounts and not resolved by a distinct third mode, our bimodal fit would classify urban rBC as South American smoke and, therefore, not affect the quantification of advected African smoke. Along these lines, the model results further suggest a rather low and constant background of anthropogenic emission (urban, traffic, etc.), but we cannot validate this in the context of the present study (Supplementary Fig. 6).

Figure 3 emphasizes that smoke from both, South American and African fires, was a major component of the aerosol population over the Amazon throughout the year. In fact, episodes with black carbon concentrations low enough to be considered as pristine atmospheric conditions[8] – i.e., $M_{rBC} < 0.01\,\mu g\,m^{-3}$ – accounted only for ~ 7% of the entire two-year measurements. South American smoke was particularly prominent throughout the dry season months from August to November, with a dry season average of $M_{rBC,SAm,dry} = 0.24 \pm 0.15\,\mu g\,m^{-3}$, which is closely related to the seasonality of the burning activities in the basin[8,44] (Fig. 3d). The smoke from South America originated from fires in different ecosystems (Supplementary Fig. 7) mainly in the dry season. Minor and rather sporadic fractions of South American smoke can also be observed during the wet season

(February to May). Remarkably, African smoke was present for most of the two years and contributed substantially to the Amazonian pollution burden. It shows a pronounced seasonality with two maxima: the first peak between January and March was associated with the long-range transport of dust and smoke from Northern Africa (refs. [21,25]), while the second peak in August and September corresponds to the long-range transport of smoke from Southern Africa[30]. The African smoke accounted for an average of $61 \pm 22\%$ of the BC burden in the wet season, with an average concentration of $M_{rBC,Afr,wet} = 0.16 \pm 0.20\,\mu g\,m^{-3}$, and contributed an average of $28 \pm 18\%$ in the dry season, with an average concentration of $M_{rBC,Afr,dry} = 0.11 \pm 0.11\,\mu g\,m^{-3}$. The seasonality of the South American and African smoke fractions agrees well with (i) the accumulated number of fires along the backward trajectories (CF_{BT}) in Fig. 3d, which is a proxy for the abundance of fires relatively close to ATTO[30] and, (ii) the CO concentrations in the westerly trade winds at the South American coast ($ROI_{offshore}$) in Fig. 3e, which is a proxy for the amount of long-range transport of African biomass burning emissions.

With this quantitative source assignment, we classified the atmospheric conditions at ATTO based on the relative contributions of both smoke sources in order to analyze the associated optical and physicochemical aerosol properties. With the fraction of African rBC in the total rBC ($M_{rBC,Afr}/M_{rBC}$) serving as a criterion, we defined four smoke regimes (i) dominant South American influence, (ii) majoritarian South American influence, (iii) majoritarian African influence, and (iv) dominant African influence, as illustrated in Fig. 3c. In addition, pristine atmospheric conditions – without detectable combustion influence (i.e., $M_{rBC} < 0.01\,\mu g\,m^{-3}$)[8] – are shown as a reference case since all measurements at ATTO include the natural aerosol
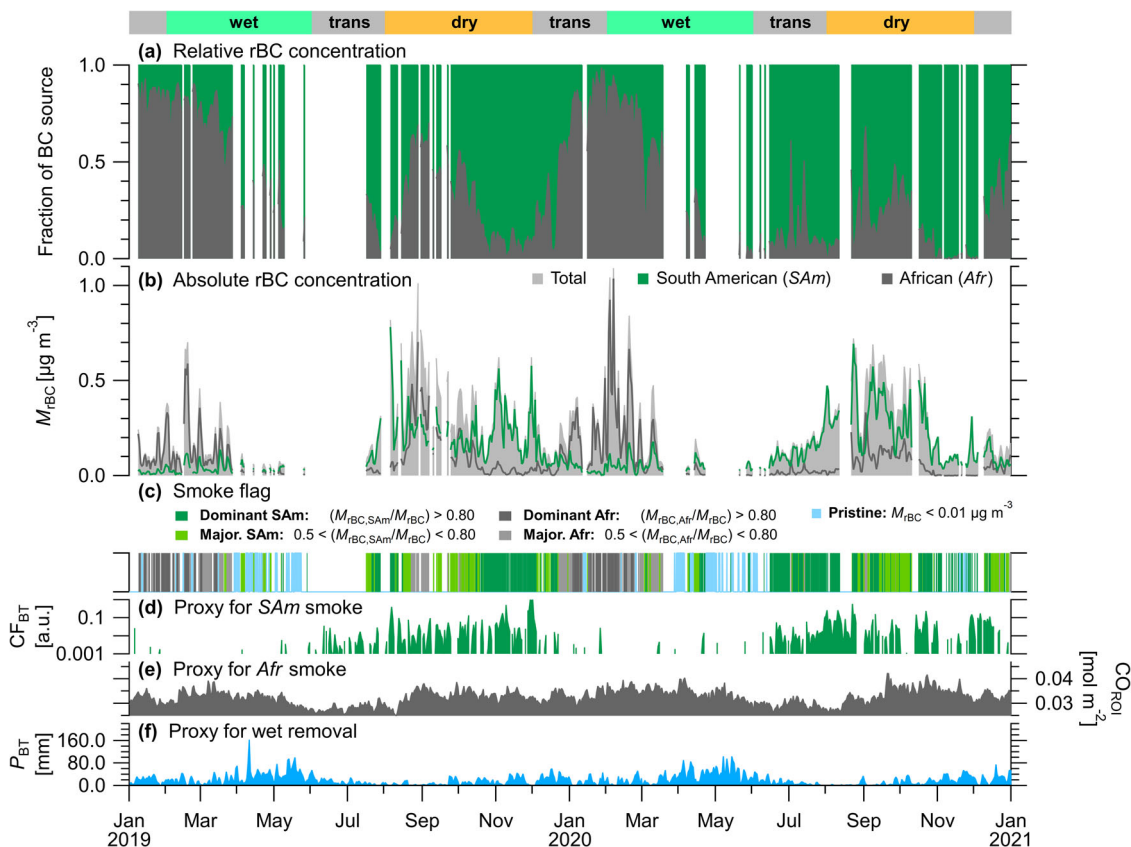
Fig. 3 Quantification of African & South American black carbon mass concentrations. Relative (**a**) and absolute (**b**) contributions of African vs South American biomass burning to total rBC mass concentration at ATTO in 2019 and 2020. **c** The colored bar code represents five flags for dominant and majoritarian South American influence, dominant and majoritarian African influence, as well as pristine aerosol conditions, which is the basis for the classification of smoke properties in Fig. 4. **d** As proxy for periods with intense South American smoke influence: cumulative number of fires, CF_{BT}, along the 3-day BTs starting at 200 m at ATTO[30]; **e** As proxy for African smoke influx into the Amazon: satellite-derived carbon monoxide (CO) concentration in an offshore region of interest off the Brazilian coast ($ROI_{offshore}$); **f** As proxy for aerosol wet scavenging in air masses arriving at ATTO: cumulative precipitation, P_{BT}, along the 3-day BTs[24]. The Amazonian seasonality is shown as colored bars on top of the time series for reference, which has been defined and used in previous studies[8,24,25,33,44,75] as follows: wet season (February to May), dry season (August to November), and transition periods (June-July and December-January).

background. In essence, Fig. 3 underlines that African smoke is a significant constituent of the atmospheric pollution in the Amazon essentially all year long and can not be neglected in corresponding analyses and modelling efforts.

The smoke regimes in Fig. 3c can serve as flags and, therefore, are of particular value to constrain fundamental aerosol properties across the continuous range of mixed pollution in central Amazonia. This approach allows to extract basic aerosol properties for the African and the South American smoke. Figure 4 shows the statistical analysis of aerosol properties for the different smoke regimes with clear gradients in microphysical, chemical, and optical aerosol parameters. The average M_{rBC} varies between 0.25 μg m-3 for the periods flagged as predominant South American influence, and 0.48 μg m^{-3} for predominant African influence (Fig. 4a), revealing the surprising observation that African fires can account for more black carbon mass in certain periods in central Amazonia than the South American fires, in spite of the much larger distance to the sources.

The trends in the total particle number concentration, N_{CN}, and the cloud condensation nuclei (CCN) number concentration at a supersaturation of 0.3%, $N_{CCN}(S = 0.3\%)$, behave differently compared to BC. Here, a predominant African smoke influence elevates N_{CN} and $N_{CCN}(S = 0.3\%)$ by a factor of two above the pristine background, whereas the predominance of South American smoke causes a concentration increase by a factor of

about ten (Fig. 4b). This implies that N_{CN} alone is not a particularly useful marker for clean conditions in the Amazon, in contrast to M_{rBC}, whose concentrations are one to two orders of magnitude greater in smoke affected than in pristine periods. Moreover, clear differences in particle number size distributions (Supplementary Fig. 15) and chemical composition of the submicron aerosol size range (Fig. 4c) are observed between the two dominant smoke types measured over the Amazon Basin. The African smoke is characterized by an rBC mass fraction of $f_{rBC,Afr} = 15 \pm 8\%$, in contrast to $f_{rBC,SAm} = 6 \pm 2\%$ for the South American smoke. Also, the organic mass fractions are remarkably different with only $f_{Org,Afr} = 60 \pm 7\%$ for the African smoke vs. $f_{Org,SAm} = 80 \pm 5\%$ for the South American smoke. The organics in all smoke plumes measured at ATTO appear completely oxidized, indicating a photochemical age of at least 9 h regardless the source region (Supplementary Fig. 14). Accordingly, the overall mass fraction of the inorganic constituents, including sulfate (SO_4^{2-}), ammonium (NH_4^+), nitrate (NO_3^-) and chloride (Cl^-), is substantially higher in the African smoke as well.

The observed gradients in Fig. 4 likely reflect differences in fuel, combustion phase, and atmospheric processing of the smoke. In terms of fuel, most of the African fires occur in grasslands, savannas, and open forests, whereas most of the South American fires – especially in the ATTO footprint region – occur in dense and humid forests (Supplementary Figs. 8 and 9). While
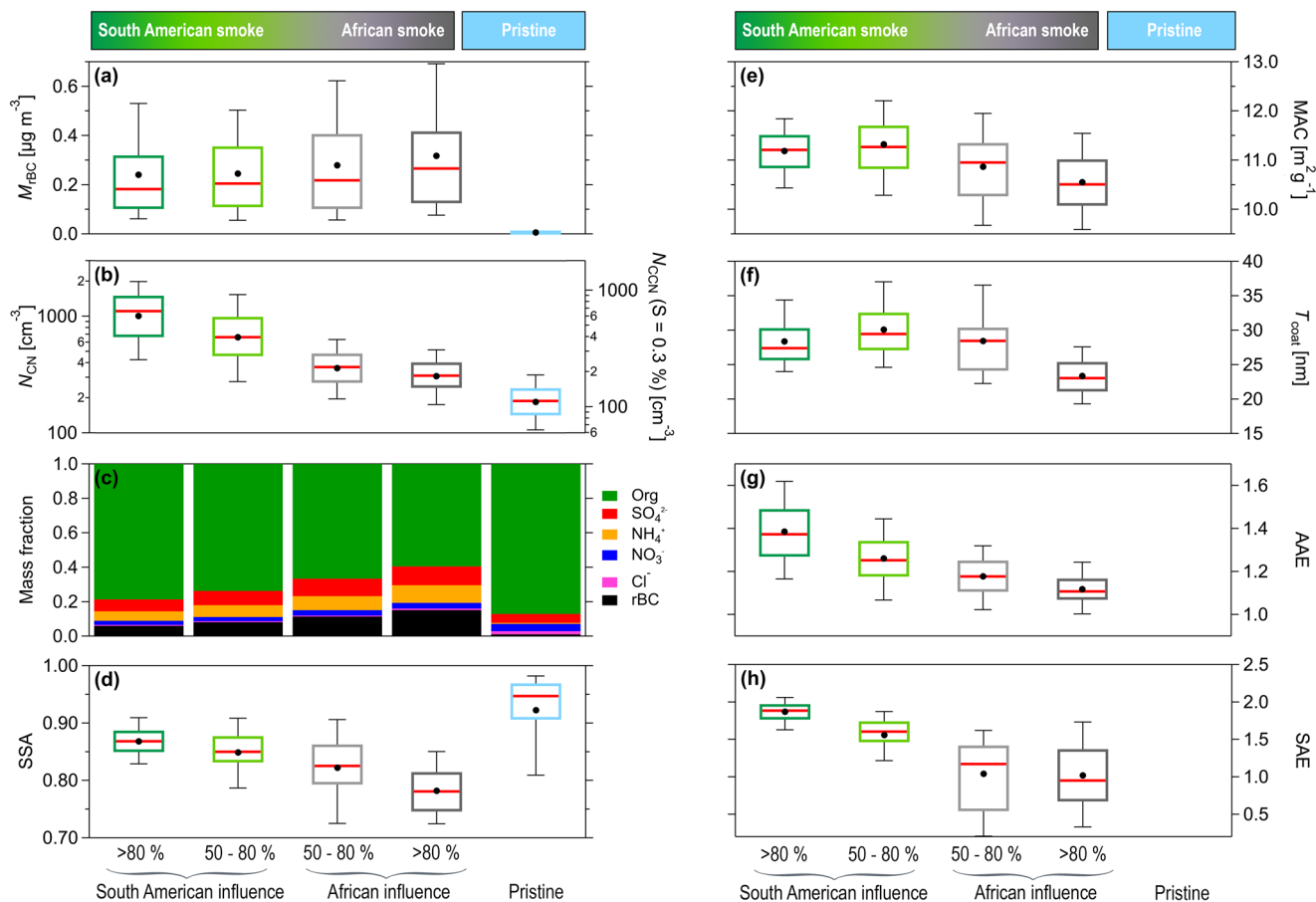
Fig. 4 Aerosol properties under African vs South American smoke influence. Statistics of selected aerosol parameters at ATTO after classification into the smoke regimes from Fig. 3c, ranging from predominant South American (green) to predominant African smoke (gray), with clear gradients in physicochemical and optical aerosol properties. **a** Mass concentration of refractory black carbon (rBC), M_{rBC}; **b** total particle number concentration > 5 nm, N_{CN} (left axis) and cloud condensation nuclei number concentration at a supersaturation of 0.3%, $N_{CCN}(S = 0.3\%)$ (right axis) calculated from the N_{CN} data (see Section "ATTO aerosol and trace gas measurements and data processing"); **c** mass fraction of the non-refractory submicrometer aerosol species organics, sulfate, ammonium, nitrate, chloride, and rBC; **d** single scattering albedo at 637 nm, SSA; **e** black carbon mass absorption cross section at 637 nm, MAC; **f** black carbon coating thickness, T_{coat}, for BC cores with ~ 180 nm < d_{MEV} < 220 nm; **g** absorption Ångström exponent, AAE (Eq. (6)); **h** scattering Ångström exponent, SAE, using the wavelength pair 450 and 635 nm (Eq. (5)). Boxes represent the 25th and 75th percentiles, the circular marker is the mean, the red horizontal bar is the median, and the whiskers are the 9th and 91st percentiles.

vegetation fires always combine flaming and smoldering combustion, African fires burning in drier fuels are dominated by flaming combustion, whereas Amazonian deforestation fires burn moister fuels and thus have a higher fraction of smoldering combustion, which is one explanation for the clear differences in f_{rBC} and f_{Org} as well as related parameters[6] (see also Supplementary Fig. 13). Moreover, photo-degradation in the course of the transatlantic transport likely causes an additional loss of organics and, thus, further lowers the f_{Org} in the African smoke[39,45].

The optical properties of the smoke depend on its microphysical parameters and are crucial for the regional radiative energy budget[46]. Clear differences between the African- and South American-dominated states were also found here. The single scattering albedo (SSA) characterizes the absorption fraction of the extinction of solar radiation by an aerosol population. Accordingly, the high f_{rBC} and low f_{Org} in the African smoke entail a rather low SSA value (at 637 nm) of $SSA_{Afr} = 0.78(0.74 - 0.81)$ (median, 25th–75th percentiles), compared to $SSA_{SAm} = 0.87(0.85 - 0.89)$ for the South American smoke with its relatively low f_{rBC} and high f_{Org} (Fig. 4d). These values are in line with previous observations of a decreasing SSA due to the influx of African aerosols into the Amazon[7,30,44] and are only slightly higher than previously

measured SSA values (660 nm) between 0.65 and 0.76 over western Africa[47]. Under pristine conditions, we found an SSA of $0.94(0.91 - 0.97)$, which is slightly below unity probably due to the presence of absorbing biogenic aerosol particles, such as pigmented fungal spores or light-absorbing organic aerosols, which are called brown carbon.

The mass absorption cross section (MAC, at 637 nm) is a fundamental input parameter to convert BC mass into BC-related absorption in climate models. We obtained $MAC_{Afr} = 10.5(10.1 - 11.0)m^2 g^{-1}$ for the African smoke and $MAC_{SAm} = 11.2(10.8 - 11.5)m^2 g^{-1}$ for the South American smoke (Fig. 4e), in good agreement with previous studies over the Amazon and the Atlantic Ocean[29,44]. All these values greatly exceed the reference value of $MAC_{ref} = 6.5 \pm 1.0 \, m^2 g^{-1}$ (at 637 nm) for uncoated black carbon particles[48]. Hence, the absorption enhancement ($E_{abs} = MAC/MAC_{ref}$) between $E_{abs} = 1.6$ for the African smoke and $E_{abs} = 1.7$ for the South American smoke can be largely attributed to the presence of coatings on the BC cores, which causes the so-called lensing effect[49]. The relation between MAC and coating thickness (T_{coat}) is in line with the similar patterns in Fig. 4e, f and Supplementary Fig. 17. In fact, most rBC particles at ATTO exhibited substantial coatings (Fig. 4f). The thickness of the coating (for ~ 180 nm < d_{MEV} < 220 nm) appears to depend

only slightly on the source and age of the smoke. The fresher South American smoke was characterized by an average coating thickness of $T_{coat,SAm} = 27(26 − 30)$nm, compared to $T_{coat,Afr} = 23(21 − 25)$nm for the more aged African smoke. The thinner coating for the aged African smoke is likely related to the photochemical degradation and evaporation of the organic compounds in the free troposphere during transatlantic transport[39,40].

Besides the coating-related lensing effect, an absorption enhancement, especially in the ultra-violet range, can be related to the presence of brown carbon (BrC)[50]. The presence of BrC entails a wavelength dependence of the absorption, which is typically expressed as the absorption Ångström exponent (AAE). Figure 4g shows that the AAE (calculated across all 7 measurement wavelengths) of South American smoke clearly exceeds unity with $AAE_{SAm} = 1.37(1.27−1.48)$, which indicates a contribution of BrC to the overall absorption[51]. Using positive deviations of AAE from unity to define BrC[52], we estimate that ~ 30% of the absorption at 370 nm is BrC-related. The contribution of brown carbon in African smoke seems much smaller (~ 10%), according to the average of $AAE_{Afr} = 1.11(1.07−1.17)$, which can be explained by the higher ratio of flaming to smouldering combustion conditions in the African burns followed by the photo-degradation of chromophores in the BrC during the transatlantic transport[38,40]. The spectral dependence of the scattering coefficient is expressed as the scattering Ångström exponent (SAE) and is related to the aerosol size distribution[53]. The differences in SAE in Fig. 4h (here calculated with the wavelength pair 450 and 635 nm through Eq. (5)) are substantial, with a high and defined $SAE_{SAm} = 1.88(1.76 − 1.97)$ for the South American smoke in contrast to the much lower and widely variable $SAE_{Afr} = 0.94(0.67−1.37)$ for the African smoke. The African SAE agrees well with the previous results from African smoke over the Atlantic – i.e., $0.59−1.64$, median of 1.07[47] – and its large variability can be explained by the co-transport of mineral dust, smoke, and sea spray aerosol, which span across a wide aerosol size range[25].

The experimentally retrieved BC concentrations and temporal variability of the South American vs African smoke fractions at ATTO agree comparatively well with the corresponding results from the global models EMAC[54] and CAM-chem[55] (Fig. 5). The agreement is particularly convincing for the South American BC, yielding a clear positive correlation (Pearson's coefficient $R \approx 0.70$) and a relatively low mean bias (MB) between − 6% and 3% (Fig. 5b), which underlines that the experimental discrimination between both smoke regimes provides an accurate representation of the pollution at ATTO. The comparison between modelled and measured African BC yields a moderate positive correlation ($R \approx 0.55$) with a rather high bias of about 50%, however, indicating that the models tend to underestimate the African smoke influx (Fig. 5c). Especially, some of the large peaks in Fig. 5c, corresponding to periods with particularly strong African smoke advection, are not well captured or even absent in model results. This comparatively large discrepancy in representing the transatlantic transport of African smoke is in line with previous studies showing that its correct representation in various models has been a challenge due to uncertainties in fire emission inventories, wet scavenging, plume rise, and subsidence parameterizations (refs. [56–59]). In this sense, the present data can serve as an experimental reference for model improvement to represent the transatlantic smoke transport.

The model results emphasize that the African smoke influx is a significant factor for the entire Amazon and even reaches the very remote and untouched western basin (Fig. 6). The African contribution to the instantaneous biomass burning-related solar radiative effect due to aerosol-radiation interactions (IRE$_{ARI}$) at ATTO is shown in Fig. 6a, which can be seen as a lower limit as

the models tend to underestimate the African influence. At ATTO, the largest IRE$_{ARI}$ values, with a dimming at the surface of up to 30 W m$^{−2}$, are related to peaks with particularly high BC concentrations under heavy smoke from South American fires. The African smoke contributes on average ~ 94% to the IRE$_{ARI}$ at ATTO (and ~ 50% for the entire basin) during the wet season as well as ~ 12% at ATTO (and ~ 6% for the entire basin) during the dry season (Fig. 6a). The African smoke clearly dominates IRE$_{ARI}$ in the eastern basin and its influence decreases towards the west (Fig. 6b, c). This implies that studies on the smoke-related radiative energy forcing in the Amazon[12,13] – particularly if focusing on the vulnerable eastern basin, where rapid transformations in the course of progressing climate and land use change are expected – must take the influence of African smoke into account.

Summary and conclusions
Biomass burning smoke occurs frequently across the entire Amazon basin, driven by land clearing and management fires in agriculture, infrastructure development, and mining. In addition, long-range transported smoke from Africa contributes to the overall aerosol burden in the Amazon, but its influence has not been quantified so far. Here, we present this quantification based on long-term SP2 measurements of rBC properties at the ATTO site in the central Amazon. Our measurements covered the years 2019 and 2020, when particularly severe burning seasons aroused public concerns worldwide. We found consistent and significant differences between BC core mass size distributions under the dominant influence of South American fires, mostly from moist rain forest regions, vs highly aged smoke from African fires. The observed properties of rBC at ATTO were in remarkable agreement with aircraft data collected within biomass burning plumes close to the sources, indicating that the rBC properties are conserved upon horizontal transport. Based on this finding, we present a refined classification scheme to quantify South American and African smoke influences at ATTO. The contribution of African smoke reveals a pronounced seasonality with two maxima, accounting for up to 60% of the rBC mass in the Amazonian dry season and up to 90% in the wet season. By comparing our observations with global models, we show that the models capture the variability of the regional sources well, but at the same time greatly underestimate the African influx. Our results indicate the urgent need to improve the model representation of transatlantic long-range transport on regional and global scales, fire emission inventories, and plume rise parameterizations. Further, our dataset provides an improved observational basis for model investigation of aerosol-cloud-radiation interactions over the Amazon Basin and the fate of African biomass burning after transatlantic transport. The efficient transport of African smoke over ~ 10000 km to the western Amazon suggests that this process likely also occurred in the preindustrial era because natural and indigenous fires have been an ancient ecological agent in the fire-prone African vegetation throughout the Holocene and Pleistocene[60]. Accordingly, biomass burning smoke has likely been an atmospheric factor of significance in the Amazon even long before the modern era of deforestation and land use change, playing important roles in the forest formation, soil fertilization, as well as carbon and water cycles[61]. Nevertheless, the ubiquity and concentrations of heavy smoke over the Amazon today is probably as unprecedented as the deforestation rates, with potentially dire consequences for regional and global climate change.

Methods
ATTO aerosol and trace gas measurements and data processing. The Amazon Tall Tower Observatory (ATTO, https://www.attoproject.org) is located in the
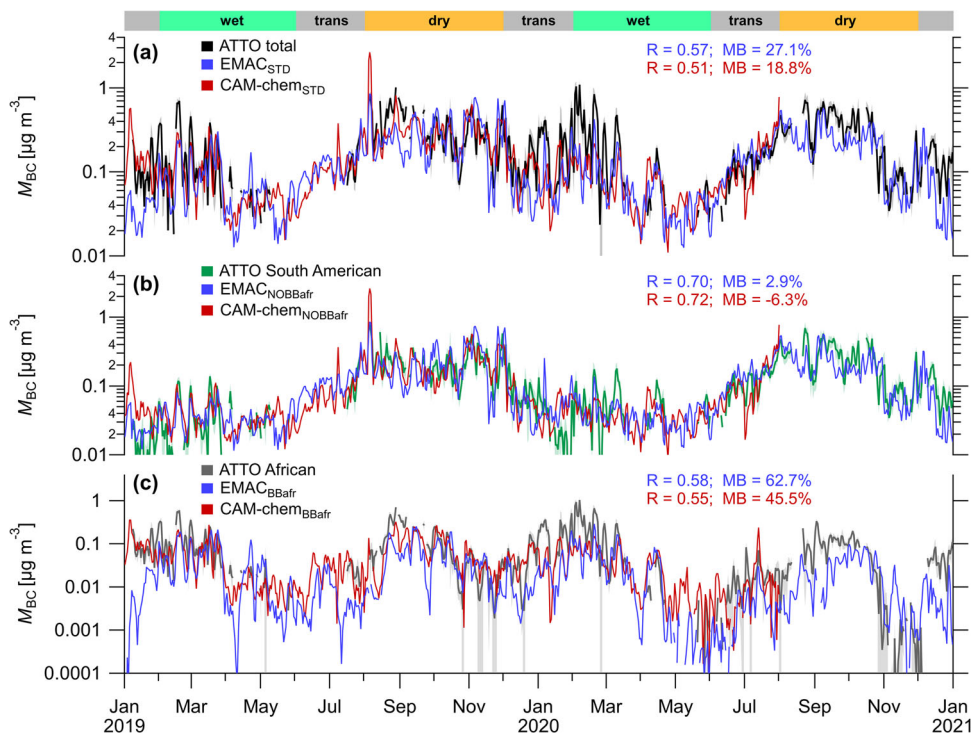
Fig. 5 Model-observation comparison. Comparison between the experimentally obtained BC mass concentrations (M_{BC}) at ATTO and corresponding simulations with the global models EMAC and CAM-chem. Daily averages of the (**a**) total BC mass concentration measured at ATTO (black line), as well as the corresponding BC concentration attributed to (**b**) South American fires (green line) and (**c**) African fires (gray line), according to the deconvolution method. The total modelled M_{BC} has been obtained from standard runs based on the entire emission inventory (M_{STD}). The modelled South American BC ($M_{NOBBafr}$) was obtained from runs with African sources switched off. The modelled African BC (M_{BBafr}) was obtained as $M_{BBafr} = M_{STD} - M_{NOBBafr}$ (for details see Sections "EMAC model" and "CAM-chem model"). The legend specifies the correlation coefficients (R) and the mean bias (MB) for the relationship between experimental and model data according to Supplementary Fig. 18.

central Amazon basin in a region with largely untouched primary rain forest (2.146° S, 59.006° W, 130 m above sea level, ~150 km northeast of Manaus, Brazil). Details on atmospheric, geographic, and ecological conditions at the ATTO site and on its footprint region can be found elsewhere[24,33]. Since 2012, the site has been operated for long-term and in-depth investigations of meteorology, trace gases, atmospheric aerosols, and rain forest ecology (refs. [44,62–64]). The measurements presented here span two full seasonal cycles, from January 2019 to December 2020. The results were obtained from a broad set of aerosol instruments, sampling from the 325 m inlet height at the tall tower. The sample air reached the air-conditioned laboratory container with the instruments through a stain-less steel tube (finetron tubes, Dockweiler AG, Neustadt-Glewe, Germany, outer diameter 25 mm, inner diameter 22.1 mm), equipped with a total suspended matter inlet head. The total air flow rate in the tube was 35 L min^{-1}. A transmission curve, specifying particles losses due to diffusion, sedimentation, and impaction in the inlet tube is shown in Supplementary Fig. 10 (see also refs. [25,65]). Particle losses in the size range most relevant for this work (i.e.,~ 50 nm to ~ 1 μm) are <5%. In the laboratory container, a custom-build isokinetic split distributed the sample air to the individual instruments. The sample air was dried by an automated condensation dryer to a relative humidity <40%. All aerosol data were corrected for standard temperature and pressure (STP, 273.15 K, 1013.25 hPa). All data were averaged to 3 h time resolution. The data processing was conducted with IGOR Pro (version 8.04, Wavemetrics, Inc., Portland, OR, USA).

Single particle soot photometer (SP2). Refractory black carbon (rBC) particles were measured by an 8-channel single-particle soot photometer (SP2, S/N 12, Droplet Measurement Technologies, Longmont, USA). The instrument measures the time-dependent scattering and incandescence signals produced by single aerosol particles when crossing an intense laser beam with a Gaussian beam profile (Nd:YAG; λ = 1064 nm)[66,67]. All particles crossing the laser beam scatter light, which is detected by avalanche photodetectors (APD). The intensity of the scattered signal is proportional to the particle scattering cross-section, from which its optical diameter (D_p) can be determined. Pure scattering particles (SC) do not absorb light and therefore remain unaffected by the passage through the beam. The particles containing rBC, however, absorb the laser radiation and are quickly heated to their vaporization temperature (~ 4000 °C), which initiates the emission of incandescence light. The peak intensity of the incandescent signal is proportional to the rBC mass in the particles (regardless of the coating). Thus, the mass-equivalent diameters of the individual rBC cores (d_{MEV}) are calculated by assuming a void-free

sphere with a BC material density of 1.8 g cm^{-3}[68]. The SP2 is sensitive to rBC-free particles in the optical size range of about 180 < D_p < 400 nm and to rBC cores in the size range of about 80 < d_{MEV} < 500 nm, with a counting efficiency close to unity. Calibrations of the incandescence and scattering channels were performed periodically (i.e., in intervals of 2-3 months) using size-selected fullerene soot (Sigma-Aldrich Inc.) and ammonium sulfate (Sigma-Aldrich Inc.) particles, respectively. Particles were generated with an aerosol nebulizer (Droplet Measurement Technologies), dried by a diffusion drier, and size-selected by a differential mobility analyzer (DMA, Grimm Aerosol Technik, Ainring, Germany). The particle masses of the DMA-selected fullerene soot particles were calculated using the effective density data provided in Gysel et al.[69]. During the long-term ATTO measurements, the SP2 software was set to record 1 in every 10 particles. The data were processed with the Paul-Scherrer Institute (PSI) SP2 toolkit[70]. Further details on the SP2 operation at ATTO can be found in Saturno et al.[44].

In order to account for the missed rBC mass below the lower detection limit of the SP2, we applied the extrapolation method recommended by Pileci et al.[71]. The correction factor spanned from 1 to 10% of the measured rBC mass for periods dominated by South American and African biomass burning, respectively.

When an internally mixed particle, with rBC core and non-absorbing coating, crosses the laser beam, the rBC-related light absorption causes rapid heating and, thus, initiates a sequential evaporation of the entire particle. First, the non-refractory coating evaporates causing a shrinkage of the particle diameter and its scattering cross section. This is followed by the evaporation of the rBC core[72]. The optical size of the whole particle prior to evaporation can be determined by fitting of a Gaussian to the leading-edge-only (LEO-fit) of the early scattering signal before the particle starts to evaporate[72]. The coating thickness is determined from the SP2's reconstructed scattering and incandescence signals, assuming a spherical concentric core-shell morphology for the Mie calculations[68]. The coating thickness (T_{coat}) is then calculated based on the difference between D_p determined from the LEO fit and d_{MEV} according to

$$T_{coat} = \frac{D_p - d_{MEV}}{2} \qquad (1)$$

For the Mie calculations, we used the refractive indices of 1.75 + 0.43i for the core and 1.50 + 0i for the coating, following Yuan et al.[73] and Motos et al.[74]. The chosen values provide good agreement between the optical diameter of the rBC cores (from the LEO-fit) and the mass-equivalent diameter. The coating-thickness
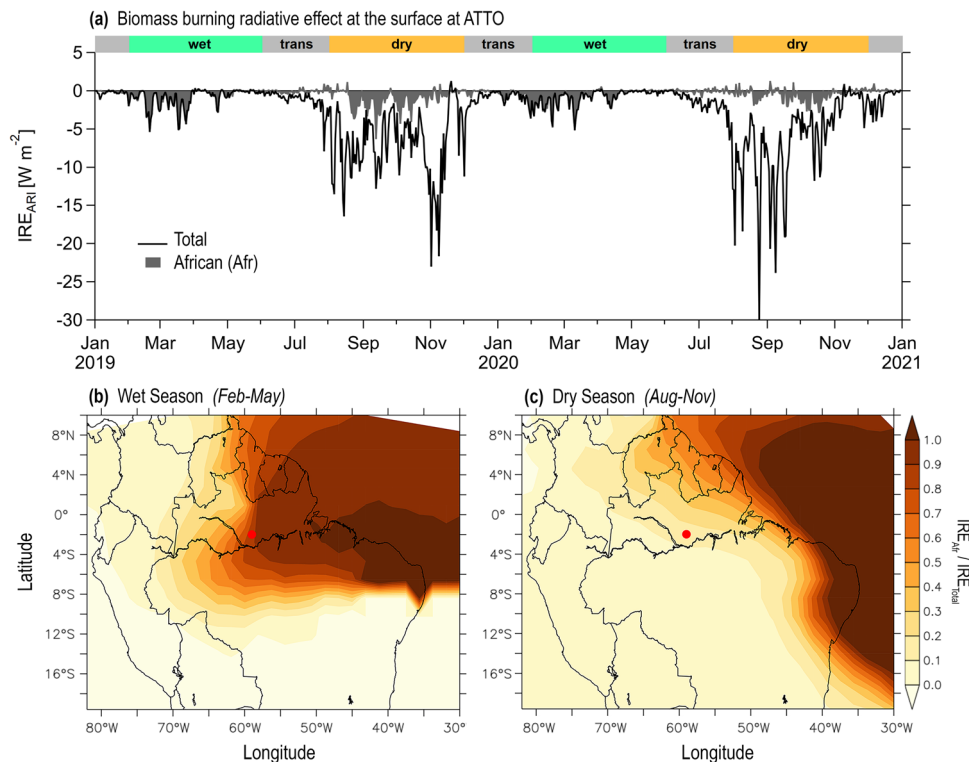
Fig. 6 African smoke influence on aerosol-radiation interactions in Amazonia. Contribution of African smoke to instantaneous radiative effect (IRE$_{ARI}$) as time series for the years 2019 and 2020 at ATTO (**a**) as well as geographically resolved for the entire Amazon basin under wet season (**b**) and the dry season conditions (**c**). In (**a**), the radiative effect – here a dimming of the surface net shortwave (SW) radiation – is shown in black for all biomass burning smoke and in gray for the African contribution. Results were obtained from the EMAC model for all-sky conditions using the standard aerosol microphysical properties from the model.

analysis in this study includes T_{coat} values from rBC cores in the selected size range $180 > d_{MEV} > 220$ nm.

Further measurements. The total aerosol particle number concentration for particles > 6 nm (N_{CN}) was measured by a Condensation Particle Counter (CPC, model 5412, Grimm Aerosol Technik, Ainring, Germany). Particle number size distributions in the size range of 10–400 nm were measured by a Scanning Mobility Particle Sizer (SMPS, classifier models 3080, 3082; CPC models 3772, 3750; Neutralizer model 3077; DMA model 3081; TSI Inc. Shoreview, MN, USA). Details on the SMPS measurements at ATTO can be found elsewhere[75–77]. The SMPS data was processed with the Aerosol Instrument Manager software (AIM, version 10, TSI Inc.). Note that during the period from 01 August to 30 September 2019, the SMPS at the 325 m inlet had technical issues and, therefore, SMPS (model 3080) data from the 60 m inlet line at the 80 m mast was used instead (for further details see ref.[75]). In terms of overall aerosol variability, the sampling heights at 325 m vs 60 m show no pronounced differences (i.e., concentration levels and mode diameters). The CCN number concentration at a supersaturation $S = 0.3\%$, $N_{CCN}(S = 0.3\%)$, was calculated from the N_{CN} data using the κ-Köhler parametrization and annually averaged error function (erf) fit parameters presented in Pöhlker et al.[75].

Carbon monoxide (CO) mixing ratios were measured with a Picarro cavity ring-down spectrometer (G1302 analyzer, Picarro Inc., Santa Clara, USA) at five different sampling heights on the 80 m walk-up tower. Here, we used CO data measured at 79 m height. Meteorological parameters such as temperature (T), relative humidity (RH), air pressure (p), precipitation rates (P), wind speed and wind direction were measured with a compact weather station (Lufft, WS600-LMB, G. Lufft Mess- und Regeltechnik GmbH, Fellbach, Germany) at a height of 321 m on the tall tower.

Aerosol chemical composition was analyzed with an Aerosol Chemical Speciation Monitor (ACSM, Aerodyne Research Inc., Billerica, MA, USA) at the 60 m height of the 80 m walk-up tower. The instrument measures the major aerosol constituents organics (Org), sulfate (SO_4^{2-}), nitrate (NO_3^-), ammonium (NH_4^+), and chloride (Cl^-)[78]. Data below the following detection limits of the ACSM (measured as described by Ng et al.[78]) were filtered out: 0.2 μg m^{-3} for Org, 0.015 μg m^{-3} for SO_4^{2-}, 0.16 μg m^{-3} for NH_4^+, 0.013 μg m^{-3} for NO_3^-, and 0.01 μg m^{-3} for Cl^-[8]. The ACSM data coverage during the wet seasons of 2019 and 2020 is comparatively sparse due to technical issues, affecting the statistical analysis of periods with dominant African smoke influence. Despite the reduced statistics, the obtained results are robust and consistent with previous observations over the

Amazon basin[79–81] as well as over the South Atlantic Ocean[38,82,83]. The total submicrometer aerosol mass (M_{PM1}) was determined as the sum of all ACSM-measured species as well as the SP2-derived rBC mass M_{rBC}. Note that NH_4^+ ranged below its detection limit during the pristine periods, which was omitted for the calculation of the mass fractions, following the approach in Pöhlker et al.[8].

The aerosol absorption coefficient (σ_{abs}) at $\lambda = 637$ nm was measured by a Multi-Angle Absorption Photometer (MAAP, model 5012, Thermo Electron Group, Waltham, USA). From 22 August 2020, the MAAP had instrumental issues causing an overestimation of the absorption coefficient; these data were not considered in the analysis. The σ_{abs} at 7 wavelengths (370, 470, 520, 590, 660, 880 and 950 nm) were measured by an aethalometer (model AE33, Aerosol d.o.o., Ljubljana, Slovenia). A correction scheme to account for instrument artefacts was applied to the aethalometer data[44,84,85]. The corrections to account for multiple scattering effects use MAAP data as a reference absorption measurement[85]. The aerosol scattering coefficients (σ_{scat}) at 3 wavelengths (450, 525, 635 nm) were measured by a nephelometer (model Aurora 3000, Ecotech Pty Ltd., Knoxfield, Australia). The instruments (i.e., nephelometer, aethalometer, MAAP, ACSM) were measuring through a PM1 cyclone (URG, model URG-2000-30EHB, Chapel Hill, USA), which defined a sharp particle size cut-point towards larger diameters. Details on the nephelometer, aethalometer, and MAAP measurements at ATTO can be found in Saturno et al.[44,85].

Derived aerosol parameters. The single scattering albedo (SSA), was calculated by the ratio between the scattering coefficient and the total extinction coefficient ($\sigma_{ext}(\lambda) = \sigma_{sca}(\lambda) + \sigma_{abs}(\lambda)$), according to

$$SSA(\lambda) = \frac{\sigma_{sca}(\lambda)}{\sigma_{ext}(\lambda)} \quad (2)$$

The mass absorption cross-section of black carbon (MAC$_{BC}$) represents the total light absorption per mass of BC and is used in climate models to convert mass concentration into absorption[46]. The MAC$_{BC}$ was derived from the light absorption coefficient at 637 nm, measured by the MAAP, and the rBC mass concentration, measured by the SP2, as follows

$$MAC_{BC} = \frac{\sigma_{abs,637}}{M_{BC}} \quad (3)$$

The wavelength dependence of aerosol light absorption or scattering is described by the Ångström exponent. The absorption and scattering Ångström exponents (AAE

and SAE) between a wavelength pair can be determined as follows

$$AAE(\lambda_1, \lambda_2) = -\frac{\ln(\sigma_{abs}(\lambda_1)/\sigma_{abs}(\lambda_2))}{\ln(\lambda_1/\lambda_2)} \quad (4)$$

and

$$SAE(\lambda_1, \lambda_2) = -\frac{\ln(\sigma_{sca}(\lambda_1)/\sigma_{sca}(\lambda_2))}{\ln(\lambda_1/\lambda_2))} \quad (5)$$

Several recent studies followed the wavelength pair approach to calculate AAE (refs. [19,73,83]). As an alternative approach[44], we applied a linear fit to the logarithm of the absorption or scattering coefficients vs the logarithm of the wavelength across the entire wavelength range to obtain the AAE and SAE as follows

$$\ln(\sigma_{abs}) = -AAE \cdot \ln(\lambda) + \ln(k_0) \quad (6)$$

and

$$\ln(\sigma_{sca}) = -SAE \cdot \ln(\lambda) + \ln(k_0) \quad (7)$$

Linear fits with $R^2 < 0.95$ were excluded from the analysis.

Aircraft measurements. Selected rBC data from two aircraft campaigns were used in this study. The measurements were conducted onboard the German High Altitude and LOng Range (HALO) research aircraft (https://www.dlr.de/content/de/missionen/halo.html, last access 30 Aug 2021), operated by the German Aerospace Center (DLR). During both campaigns, the same set of instruments in the HALO CCN-Rack was used, which supports the direct comparability of both datasets[18]. The German-Brazilian ACRIDICON–CHUVA (Aerosol, Cloud, Precipitation, and Radiation Interactions and Dynamics of Convective Cloud Systems-Cloud Processes of the Main Precipitation Systems in Brazil: A Contribution to Cloud Resolving Modeling and to the Global Precipitation Measurement) campaign was conducted in September and October 2014, covering a large extent of the Amazon basin and the offshore region at the northeastern Brazilian coast (approx. 12°S–2°N, 79°W–49°W). The CAFE-Africa (Chemistry of the Atmosphere Field Experiment in Africa) campaign took place in August and September 2018 over the central and southern Atlantic Ocean and Western Africa with base at Sal international airport, Cabo Verde (16.75° N, 22.95° W). In this study, we focused on the CAFE-Africa flights CA04, CA05, CA12, CA13, and CA15 over the South Atlantic Ocean (approx. 10°S–15°N, 35°E–5°E), where African biomass burning layers were intensively probed. Detailed information on the ACRIDICON–CHUVA and CAFE-Africa campaigns can be found elsewhere[18,34,79,86,87]. The regions/locations where biomass burning plumes were encountered are shown in Fig. 1.

Biomass burning aerosol source assignment using the SP2. The biomass-burning smoke in the Amazon can be regarded as a mixture from South American and African fires with a high spatiotemporal variability of both influences (refs. [23,25,26,30,44,88]). Related to the approach by Liu et al.[31], we used differences in the rBC microphysical properties for a source assignment of the biomass burning smoke measured at ATTO. We found that the size distributions of the rBC cores (geometric mean diameters, D_{rBC}, and the geometric standard deviation, σ_{rBC}) show statistically different properties (Fig. 1), which are conserved upon horizontal transport, allowing a discrimination of African vs South American BB influences. Here we show that the rBC mass size distributions at ATTO can be deconvoluted quantitatively as mixed South American and African influences by conducting a bimodal fitting to the 3 h averaged rBC mass size distribution. The fit was applied across the rBC size range from 90 to 500 nm. The following function according to Heintzenberg[89] has been used:

$$f(d_{MEV}) = \frac{A_{rBC,SAm}}{\sqrt{2\pi}\log(\sigma_{rBC,SAm})}\exp\left[-\frac{(\log(d_{MEV})-\log D_{rBC,SAm})^2}{2\log^2(\sigma_{rBC,SAm})}\right] + \frac{A_{rBC,Afr}}{\sqrt{2\pi}\log(\sigma_{rBC,Afr})}\exp\left[-\frac{(\log(d_{MEV})-\log D_{rBC,Afr})^2}{2\log^2(\sigma_{rBC,Afr})}\right] \quad (8)$$

with the fit parameters $D_{rBC,i}$ as geometric mean diameter, $\sigma_{rBC,i}$ as geometric standard deviation, and $A_{rBC,i}$ as the rBC mass concentration at $D_{rBC,i}$. The bimodal fit comprised one African (Afr) mode and one South American (SAm) mode. The fit parameters $D_{rBC,i}$ and $\sigma_{rBC,i}$ were constrained according to the rBC properties for largely pure African and South American smoke (Supplementary Fig. 4). Specifically, the following constraints were used for the African mode:

1. $A_{rBC,Afr}$ was a free parameter
2. $D_{rBC,Afr}$ was constrained within the range from 215 to 219 nm
3. $\sigma_{rBC,Afr}$ was constrained within the range from 1.47 to 1.49

The following constraints were used for the South American mode:

1. $A_{rBC,SAm}$ was a free parameter
2. $D_{rBC,SAm}$ was constrained within the range from 176 to 185 nm
3. $\sigma_{rBC,SAm}$ was constrained within the range from 1.64 to 1.69

Based on the bimodal fits, the African ($M_{rBC,Afr}$) vs South American ($M_{rBC,SAm}$) contributions to the total M_{rBC} were quantified as the integral of the corresponding modes over the full size range. This include potential tails outside the SP2 detection range, however, this represents only a small contribution. For illustration, examples of bimodal-fitted rBC size distributions for different mixed smoke conditions are

shown in Supplementary Fig. 5. Only successful fits ($R^2 > 0.95$) were considered for further analysis. The resulting time series of the separated influence of African vs South American rBC based on this approach, which we refer to as the deconvolution method, is shown in Fig. 3. A detailed description and rationale of the method, can be found in the Supplementary Note 1.

Based on the relative contribution of South America and African smoke, the aerosol properties at ATTO were classified into the following five pollution regimes:

1. Dominant South American influence: $M_{rBC,SAm}/M_{rBC} > 0.80$
2. Majoritarian South American influence: $0.5 < M_{rBC,SAm}/M_{rBC} < 0.80$
3. Majoritarian African influence: $0.5 < M_{rBC,Afr}/M_{rBC} < 0.80$
4. Dominant African influence: $M_{rBC,Afr}/M_{rBC} > 0.80$
5. Pristine: $M_{rBC} < 0.01\ \mu g\ m^{-3}$ according to the definition in Pöhlker et al.[8]

Backward trajectories. The backward trajectory (BT) analysis is based on the Hybrid Single-Particle Lagrangian Integrated Trajectory model (HYSPLIT, NOAA-ARL) with meteorological input data from the Global Data Assimilation System[90,91]. The 3 d BTs in the composite maps (e.g., Fig. 2) were calculated with GDAS meteorological input data at 0.25° resolution. A starting height of 200 m a.g.l. (above ground level) was chosen. For a systematic ATTO-related BT analysis, refer to Pöhlker et al.[24].

Proxy for African smoke influx into the Amazon: satellite-derived CO column density in a region off the South American coast. To estimate the influx of air masses carrying African biomass burning emissions into the Amazon basin, the carbon monoxide data from the satellite Sentinel-5P (vertically integrated CO column density in mol m^{-2}; OFFL L3 product; obtained through Google Earth Engine, https://code.earthengine.google.com/, last access 06 Apr 2022) within an offshore region of interest ($ROI_{offshore}$) located at the northeastern coast of South America was used. The $ROI_{offshore}$ and the corresponding CO data (CO_{ROI}) are shown in Supplementary Fig. 11. The CO_{ROI} time series is further shown in Fig. 3e and Supplementary Fig. 3a in relation to the ATTO data. In the steady westerly trade winds[24,30] the influx of African smoke into the central Amazon passes through the $ROI_{offshore}$, which makes CO_{ROI} a useful (qualitative) marker for its seasonality. For typical air mass velocities (obtained from the length of the BTs), the average transport time from the center of the $ROI_{offshore}$ to ATTO is about 3.2 days. Accordingly, the CO_{ROI} time series was shifted by 3.2 days. Note that this average shift is just an approximation since the offset time can vary quite significantly, depending on wind speed.

Proxy for periods with intense South American smoke influence at ATTO: cumulative number of fires along backward trajectories. The time series of cumulative fire intensity along the BTs (CF_{BT}) was calculated based on (i) an ensemble of filtered 3 d HYSPLIT BTs, started every hour in the time frame between 1 January 2019 and 31 December 2020, at a starting height of 200 m, and (ii) daily georeferenced fire intensity maps, in W m^{-2}, from the Global Fire Assimilation System (GFAS). Detailed information on this procedure can be found in Holanda[30]. The GFAS fire intensity maps were obtained as NetCDF3 files with a spatial resolution of 0.1° latitude by 0.1° longitude. Only those segments of the individual BTs in convective exchange with the surface/fires (i.e., BT segments with heights < 1000 m) and encountering en route convection (i.e., BT segments with solar radiation fluxes > 50 W m^{-2}) were included in the calculation of CF_{BT}. In addition, the individual BTs were terminated upon en route occurrence of rain (i.e., for rainfall > 2 mm). Details of the BT data set and filtering can be found in Pöhlker et al.[24]. Details on the calculation of CF_{BT} can be found in Holanda et al.[30]. The CF_{BT} time series is shown in Fig. 3d and Supplementary Fig. 3b in relation to the ATTO data.

Proxy for aerosol wet scavenging in air masses arriving at ATTO: cumulative precipitation along backward trajectories. Precipitation data, which was available through GDAS and the HYSPLIT model for every data point of the BTs, was used to calculate the cumulative precipitation, P_{BT}, for every individual 3-day BT. The resulting P_{BT} time series represents the amount of rain that the air masses experienced during their last 3 days of transport towards ATTO. Accordingly, P_{BT} reflects the extent of rain-related aerosol scavenging of the arriving air masses. For details, refer to Moran-Zuloaga et al.[25] and Pöhlker et al.[24]. The CF_{BT} time series is shown in Fig. 3f and Supplementary Fig. 3c in relation to the ATTO data.

Geographic information system (GIS) data and processing. The analysis of geographic information system (GIS) data sets was conducted with the QGIS software package (version 3.12, QGIS development team, https://www.qgis.org/, last access 07 Apr 2022) using the coordinate reference of the World Geodetic System from 1984 (WGS84). The following GIS data sets have been used in this study:

1. Land cover: The land cover data was obtained from the Copernicus Global Land Service and data was downloaded under https://land.copernicus.eu/global/products/lc (last access 06 Feb 2021, ©European Union, Copernicus Land Monitoring Service <year>, European Environment Agency)."

2. Fire maps: The satellite-detected fires were obtained from the Instituto Nacional de Pesquisas Espaciais (INPE), available under http://queimadas.dgi.inpe.br/queimadas/portal (last access 07 Apr 2022). Only fires from the NASA satellites Terra and Aqua we taken into account here.

3. Wind vector fields: Wind vectors were calculated based on data from the Modern-Era Retrospective analysis for Research and Applications Version 2 model (MERRA-2, https://gmao.gsfc.nasa.gov/reanalysis/MERRA-2/, last access: 07 Apr 2022) obtained through the Giovanni online data system (https://giovanni.gsfc.nasa.gov/giovanni/, last access 07 Apr 2022).

4. Corrected reflectance satellite images: Satellite images (here from Suomi NPP / VIIRS) were downloaded as GeoTiff files from the NASA's EOSDIS Worldview site (https://worldview.earthdata.nasa.gov, last access: 07 Apr 2022).

5. Global water bodies: Maps of global water bodies were obtained from the European Space Agency (ESA) (https://www.esa-landcover-cci.org/?q=node/162, last access: 07 Apr 2022).

6. Major roads: The GIS information on highways and roads in the Amazon Basin were retrieved from the OpenStreetMap (OSM) data set (https://www.openstreetmap.org, last access 07 Apr 2022), available under the Open Database License, and the Amazonian road network from CRS maps (http://maps.csr.ufmg.br, last access 07 Apr 2022).

7. Brazilian biomes: The GIS data specifying the geographic extent of the Brazilian biomes Amazônia, Cerrado, Caatinga, and Mata Atlântica were obtained from Global Forest Watch (https://data.globalforestwatch.org, last access 07 Apr 2022). Overall, Brazil comprises six continental biomes: Amazônia, Cerrado, Caatinga, Mata Atlântica, Pantanal and Pampa. As shown in Supplementary Fig. 8, the ATTO footprint region covers four of them (in the order of their relevance for the ATTO measurements): Amazônia, Cerrado, Caatinga, and Mata Atlântica[24].

Analysis of fires per land cover type to determine mixture of burnt fuels/vegetation. In QGIS, the INPE fire maps (from the satellites Aqua and Terra only) for 2019 were projected onto the Copernicus land cover maps for 2019. The detected fires were classified into the established 22 land cover categories. The seasonality in the occurrence of land-cover-specific fires was then analyzed for the year 2019 to create Supplementary Figs. 8, 9. For Africa, this analysis was further separated into the Northern vs Southern hemisphere of the continent. For South America – and specifically for the ATTO-relevant footprint region – the fire maps were further subdivided into the biome regions Amazônia, Cerrado, Caatinga, and Mata Atlântica. Based on this seasonal data for 2019, the following periods were highlighted in Pie charts: (i) Average fire/fuel mixture in Northern Africa between January and March, which corresponds to the peak of long-range transport of African dust and smoke into the Amazon during the wet season as outlined in Moran-Zuloaga et al.[25] (Supplementary Fig. 9c2). (ii) Average fire/fuel mixture in Southern Africa between August and September, which corresponds to the peak of long-range transport of African smoke into the Amazon during the dry season as outlined in Holanda et al.[30] (Supplementary Fig. 9d2). (iii) Average fire/fuel mixtures in the ATTO footprint region in South America – separated into the four relevant biomes Amazônia, Cerrado, Caatinga, and Mata Atlântica – between August and September, which corresponds to the peak of biomass burning in the Amazon as outlined in Pöhlker et al.[24] (Supplementary Fig. 8c2–f2).

EMAC model. We used the EMAC global atmospheric chemistry model at T63 grid resolution, which has a spatial resolution of 1.8° × 1.8°, with 47 hybrid vertical levels up to 0.01 hPa[54,92–95]. The 5th generation European Centre Hamburg general circulation model (ECHAM5) was used as the base atmospheric model. Multiple submodels in EMAC represent the tropospheric and stratospheric processes and their interaction with the biosphere. We used the Modular Earth Submodel System (MESSy, v.2.55,[93,96]) to link submodels that describe emission, aerosol formation, atmospheric chemistry, clouds and other processes in the base model. The GMXe (Global Modal Aerosol Extension) submodel[97] simulates the microphysical processes in aerosols and the gas/aerosol portioning. In this set-up, we used GMXe with 7 modes, 4 hydrophilic (coarse, accumulation, Aitken and nucleation) and 4 hydrophobic (coarse, accumulation and Aitken), analogous to[94,97]. Black carbon was emitted in the accumulation and Aitken modes following a recent study[98]. The ORACLE (Organic Aerosol Composition and Evolution) submodel[99,100] was used to simulate the atmospheric evolution, composition and transport of organic aerosols. The AEROPT (AERosol OPTical properties) submodel[94,101–103], was used to simulate the aerosol optical properties. AEROPT assumes the aerosol components in each mode to be spherical, well mixed and with volume averaged refractive indices. The gas phase and heterogeneous chemistry was simulated with the MECCA submodel[104,105]. To enable the high-frequency output of data from the model at the geographic coordinates of ATTO, we implemented the SCOUT[93] submodel. Apart from these submodels, the following MESSy submodels were enabled, AIRSEA, BIOBURN, CLOUD, CLOUDOPT, CONVEC, CVTRANS, DDEP, E5VDIFF, H2O, JVAL, LNOX, OFFEMIS, ONEMIS, ORBIT, SCAV, SEDI, SORBIT, SURFACE, TNUDGE and TROPOP. Explicit description of each of these submodels can be found in the MESSy submodel list

(https://www.messy-interface.org/current/auto/messy_submodels.html, last access 28 July 2021).

The EMAC global simulations, nudged towards the ERA-5 meteorological re-analyses, were performed from January 2019 to December 2020. Over the past decade, EMAC model simulations of aerosols and trace gases have been extensively assessed against ground measurements and satellite retrievals[106–112]. Here, we use the monthly varying Community Emissions Data System (CEDS) anthropogenic emission inventory of 2014,[113] at 0.5° × 0.5° resolution for the primary emitted species, i.e. SO_2 (sulfur dioxide), NH_3 (ammonia), CO (carbon monoxide), NO_2 (oxides of nitrogen), BC, OC (organic carbon), and NMVOCs (non methane volatile organic compounds). The CEDS emission inventory includes eight broad anthropogenic source sectors – transportation (TRA), industrial combustion and processes (IND), power generation (PGN), residential and commercial combustion (RES), waste incineration (WST), agricultural waste burning (AWB), agricultural soils (AGS) and shipping (SHP). Biomass burning emissions were obtained from the Global Fire Assimilation System (GFAS) inventory[114] for the study period, with updated emission factors for fire types and chemical species from Andreae[6]. To account for the higher biomass burning emissions inventoried by the Quick Fire Emissions Dataset (QFED), used in a subsequent modelling exercise, we doubled the BC emissions in GFAS following a recent study[115]. The emissions data were then pre-processed and vertically distributed in six emission heights following Pozzer et al.[94]. Besides the standard simulation (STD) with all emissions in all geographies turned on, we performed five sensitivity simulations:

(a) NOANTH: with emissions from TRA, IND, PGN, RES, WST, AWB, AGS and SHP switched off to quantify the impact of these anthropogenic sources on the ATTO site.

(b) NOBB: with zero biomass burning emissions globally, which indicates the influence of all biomass burning emissions over the ATTO site.

(c) NOBBafr: with zero biomass burning emissions over the African continent. This test run helps to identify the impact of transported BC from African continent in the Amazon.

(d) NOBBcer: with zero biomass burning emissions from Cerrado biome.

(e) NOBBcaa: zero biomass burning emission over from Caatinga biome. The two last runs test the influence of savanna-like fires in Caatinga and Cerrado on the rBC classification scheme presented in this study.

Further, the BC influences attributed to anthropogenic pollution (ANTH), biomass burning (BB), Africa fires (BBafr), Cerrado fires (BBcer), Caatinga fires (BBcaa) and Amazonia fires (BBamz) were calculated as follow:

(a) ANTH: STD - NOANTH
(b) BB: STD - NOBB
(c) BBafr: STD - NOBBafr
(d) BBcer: STD - NOBBcer
(e) BBcaa: STD - NOBBcaa
(f) BBamz: STD - NOBB - NOBBafr - NOBBcer - NOBBcaa. This is an approximation for the fires in Amazonia since *BBamz* may have a contribution from BB from the rest of the world. However, this contribution is very small and can be ignored for our analysis.

To evaluate the ability of the models in reproducing the BC observations at ATTO, we calculated the mean bias (MB) of the model as follows

$$\text{MB}\,(\%) = \frac{\frac{\sum_{i=1}^N O_i}{N} - \frac{\sum_{i=1}^N M_i}{N}}{\frac{\sum_{i=1}^N O_i}{N}} * 100 \qquad (9)$$

where N is the number of observations, M_i and O_i are the model and observation values at each time step i, respectively.

The instantaneous (time of observations) radiative effect due to aerosol-radiation interactions for the biomass burning related emissions only (IRE_{ARI}), was calculated by the difference between the STD and NOBB model simulations

$$IRE_{ARI} = (F_{STD} - F_{NOBB}) \qquad (10)$$

where F represents the radiative flux at surface. Rapid adjustments induced by absorbing aerosol layers aloft that change atmospheric heating rates are not included here. The IRE_{ARI} was calculated using the standard aerosol parametrization from the model. The aerosol microphysical properties were not constrained by the ATTO measurements, since it does not allow having a full description of the aerosols status (such as composition for all size ranges, solubility and liquid water content) over the full period of time and for the different atmospheric levels. However, the model simulations in this configuration have been extensively evaluated in the last years against multiple observations, increasing the confidence in their numerical results[108,110,116–118].

CAM-chem model. The Community Atmosphere Model with Chemistry (CAM-chem, v.6.3) was implemented to simulate the contribution from African biomass burning to the black carbon concentration at the ATTO site. CAM-chem is an active atmosphere component of the Community Earth System Model (CESM)[55] in which a Finite Volume (FV) dynamical core[119] was coupled with the Model for Ozone and Related chemical Tracers with Tropospheric and Stratospheric chemistry (MOZART-TS1)[120] and the four-mode version of the Modal Aerosol Module

(MAM4)[121]. CAM-chem was run with a horizontal resolution of 0.94° × 1.25°, and 56 levels vertical levels to ~ 45 km while its model meteorology (including winds, surface pressure, and temperature) was nudged toward MERRA2 reanalysis (https://doi.org/10.5065/XVAQ-2X07, last access 18 August 2021). Lower boundary conditions about sea and sea ice were prescribed with the merged Hadley-OI sea surface temperature and sea ice concentration data[122].

CAM-chem has a full consideration of different processes that affect aerosol properties, including new particle formation, gas- and aqueous-phase chemistry, dry deposition and gravitational settling, water uptake, in-cloud (nucleation) and below-cloud scavenging, and release from evaporated cloud and raindrops. Anthropogenic emission of BC was extracted from Community Emissions Data System (CEDS)[113], while biomass burning emission was provided by Quick Fire Emissions Dataset (QFED)[123]. Both anthropogenic and biomass burning BC was emitted into the first model layer without considering plume rise.

The standard model simulation (CAM-chem$_{STD}$) was carried out with all emissions in all geographies activated. The simulated mass concentration of BC was then interpolated to the ATTO station position to compare with the observations. Also, to quantify the contribution of African biomass burning, a parallel experiment (CAM-chem$_{NOBBafr}$) was performed by zeroing out biomass burning emissions over the African continent. Both simulations were run from October 2018 to July 2020, where results of the first 3 months were used for spin-up.

MERRA-2. Modern-Era Retrospective analysis for Research and Applications v.2 (MERRA-2) simulated BC mass concentrations were retrieved over the bounded area (-60 < Lon < -58.125° E; -2.5 < Lat < -1.5° N) that includes the ATTO site. The area-averaged black carbon surface mass concentration with 1 h time resolution was obtained from the Giovanni platform (https://giovanni.gsfc.nasa.gov/giovanni/, last access: 23 March 2021). MERRA-2 provides near-real-time climate analysis, in which aerosol and meteorological observations are jointly assimilated within a global data assimilation system[124]. The Goddard Global Ozone Chemistry Aerosol Radiation and Transport (GOCART) model[125,126] coupled with the Goddard Earth Observing System version 5 (GEOS-5) atmospheric model[127] treats the sources, sinks, and chemistry of five externally mixed aerosol species, including dust, sea salt, black carbon (hydrophobic and hydrophilic), organic carbon, and sulfate. The GEOS-5 model runs on 0.625° × 0.5° latitude-longitude grids and 72 vertical layers from the surface to 0.01 hPa[128–130].

Biomass burning emissions of several species in MERRA-2 derive from a variety of inventories over the course of the reanalysis. Since 2010, MERRA-2 utilizes the Quick Fire Emissions Dataset (QFED) version 2.4-r6[123] which draws on the cloud correction method used in the Global Fire Assimilation System (GFAS; Kaiser et al.[114]) and employs a treatment of emissions from non-observed land areas[123]. The fire locations and fire radiative power (FRP) are obtained from MODIS level-2 fire and geolocation products. Level-2 fire products are gridded at 0.3125° × 0.25° latitude-longitude resolution and combined in order to create daily mean emissions at the same resolution. The losses for all aerosol types include dry deposition (including gravitational settling), large-scale wet removal, and convective scavenging. The model-generated precipitation is corrected with observations prior to affecting the wet deposition of aerosols over land and ocean[131]. Aerosol hygroscopic growth depends on simulated relative humidity and is considered in computations of particle fall velocity, deposition velocity, and optical parameters. Numerous studies have demonstrated the skill of the GOCART aerosol module in simulating AOD and other observable aerosol properties (refs. [126,132–134]).

Data availability

The datasets presented here are available under https://doi.org/10.17617/3.YTLQYH[135]. Additional ATTO data can be found in the ATTO data portal under https://www.attodata.org/.

Code availability

The Modular Earth Submodel System (MESSy) is continuously further developed and applied by a consortium of institutions (MESSy, 2023). The usage of MESSy and access to the source code is licensed to all affiliates of institutions which are members of the MESSy Consortium. Institutions can become a member of the MESSy Consortium by signing the MESSy Memorandum of Understanding. More information can be found on the MESSy Consortium Website (http://www.messy-interface.org, last access: 14 March 2023).

References

1. Heckenberger, M. J. et al. Amazonia 1492: Pristine forest or cultural parkland? *Science* **301**, 1710–1714 (2003).
2. Fearnside, P. M. Deforestation in Brazilian Amazonia: History, rates, and consequences. *Conservation Biol.* **19**, 680–688 (2005).
3. Silva Junior, C. H. L. et al. The Brazilian Amazon deforestation rate in 2020 is the greatest of the decade. *Nature Ecol. Evol.* **5**, 144–145 (2021).
4. Pereira, G. M. et al. Physical and chemical characterization of the 2019 "black rain" event in the Metropolitan Area of São Paulo, Brazil. *Atmos. Environ.* **248**, 118229 (2021).
5. Davidson, E. A. et al. The Amazon basin in transition. *Nature* **481**, 321–328 (2012).
6. Andreae, M. O. Emission of trace gases and aerosols from biomass burning – an updated assessment. *Atmos. Chem. Phys.* **19**, 8523–8546 (2019).
7. Artaxo, P. et al. Atmospheric aerosols in Amazonia and land use change: from natural biogenic to biomass burning conditions. *Faraday Discussions.* **165**, 203–235 (2013).
8. Pöhlker, M. L. et al. Long-term observations of cloud condensation nuclei over the Amazon rain forest – part 2: Variability and characteristics of biomass burning, long-range transport, and pristine rain forest aerosols. *Atmos. Chem. Phys.* **18**, 10289–10331 (2018).
9. Roberts, G. C., Nenes, A., Seinfeld, J. H. & Andreae, M. O. Impact of biomass burning on cloud properties in the Amazon basin. *J. Geophys. Res Atmos.* **108**. https://agupubs.onlinelibrary.wiley.com/doi/abs/10.1029/2001JD000985. https://agupubs.onlinelibrary.wiley.com/doi/pdf/10.1029/2001JD000985 (2003).
10. Koren, I., Kaufman, Y. J., Remer, L. A. & Martins, J. V. Measurement of the effect of Amazon smoke on inhibition of cloud formation. *Science* **303**, 1342–1345 (2004).
11. Salati, E. & Vose, P. B. Amazon Basin: A System in Equilibrium. *Science* **225**, 129–138 (1984).
12. Liu, L. et al. Impact of biomass burning aerosols on radiation, clouds, and precipitation over the Amazon during the dry season: dependence of aerosol-cloud and aerosol-radiation interactions on aerosol loading. *Atmos. Chem. Phys.* **20**, 1–50 (2020).
13. Herbert, R., Stier, P. & Dagan, G. Isolating large-scale smoke impacts on cloud and precipitation processes over the Amazon with convection permitting resolution. *J. Geophys. Res. Atmos.* **126**, e2021JD034615 (2021).
14. Dominguez, F. et al. Amazonian moisture recycling revisited using wrf with water vapor tracers. *J. Geophys. Res. Atmos.* **127**, e2021JD035259 (2022).
15. Andreae, M. O. et al. Smoking rain clouds over the Amazon. *Science* **303**, 1337–1342 (2004).
16. Rosenfeld, D. et al. Flood or drought: How do aerosols affect precipitation? *Science* **321**, 1309–1313 (2008).
17. Aragao, L. et al. Interactions between rainfall, deforestation and fires during recent years in the Brazilian Amazonia. *Philosophical Trans. Royal Society B-Biol. Sci.* **363**, 1779–1785 (2008).
18. Wendisch, M. et al. ACRIDICON–CHUVA campaign: Studying tropical deep convective clouds and precipitation over Amazonia using the new German research aircraft HALO. *Bulletin American Meteorol. Society.* **97**, 1885–1908 (2016).
19. Darbyshire, E. et al. The vertical distribution of biomass burning pollution over tropical South America from aircraft in situ measurements during SAMBBA. *Atmos. Chem. Phys.* **19**, 5771–5790 (2019).
20. Talbot, R. W. et al. Aerosol Chemistry During the Wet Season in Central Amazonia : The Influence of Long-Range Transport. *Journal of Geophys. Res.* **95**, 16955–16969 (1990).
21. Swap, R., Garstang, M., Greco, S., Talbot, R. & Kallberg, P. Saharan dust in the Amazon basin. *Tellus Series B-Chem. Phys. Meteorol.* **44**, 133–149 (1992).
22. Baars, H. et al. Further evidence for significant smoke transport from Africa to Amazonia. *Geophys. Res. Lett.* **38**, L20802 (2011).
23. Barkley, A. E. et al. African biomass burning is a substantial source of phosphorus deposition to the Amazon, Tropical Atlantic Ocean, and Southern Ocean. *Proc. Natl Acad. Sci.* **116**, 16216–16221 (2019).
24. Pöhlker, C. et al. Land cover and its transformation in the backward trajectory footprint region of the Amazon Tall Tower Observatory. *Atmos. Chem. Phys.* **19**, 8425–8470 (2019).
25. Moran-Zuloaga, D. et al. Long-term study on coarse mode aerosols in the Amazon rain forest with the frequent intrusion of Saharan dust plumes. *Atmos. Chem. Phys.* **18**, 10055–10088 (2018).
26. Wang, Q. et al. Modeling investigation of light-absorbing aerosols in the Amazon Basin during the wet season. *Atmos. Chem. Phys.* **16**, 14775–14794 (2016).
27. Andreae, M. O. et al. Influence of plumes from biomass burning on atmospheric chemistry over the equatorial and tropical South Atlantic during CITE 3. *J. Geophys. Res.* **99**, 12793 (1994).
28. Adebiyi, A. A. & Zuidema, P. The role of the southern African easterly jet in modifying the southeast Atlantic aerosol and cloud environments. *Quarterly J. Royal Meteorol. Society.* **142**, 1574–1589 (2016).
29. Zuidema, P. et al. The Ascension Island Boundary Layer in the Remote Southeast Atlantic is Often Smoky. *Geophys. Res. Lett.* **45**, 4456–4465 (2018).

30. Holanda, B. A. et al. Influx of African biomass burning aerosol during the Amazonian dry season through layered transatlantic transport of black carbon-rich smoke. *Atmos. Chem. Phys.* **20**, 4757–4785 (2020).

31. Liu, D. et al. Size distribution, mixing state and source apportionment of black carbon aerosol in London during wintertime. *Atmos. Chem. Phys.* **14**, 10061–10084 (2014).

32. Petzold, A. et al. Recommendations for reporting "black carbon" measurements. *Atmos. Chem. Phys.* **13**, 8365–8379 (2013).

33. Andreae, M. O. et al. The Amazon Tall Tower Observatory (ATTO): Overview of pilot measurements on ecosystem ecology, meteorology, trace gases, and aerosols. *Atmos. Chem. Phys.* **15**, 10723–10776 (2015).

34. Tadic, I. et al. Central role of nitric oxide in ozone production in the upper tropical troposphere over the Atlantic Ocean and western Africa. *Atmos. Chem. Phys.* **21**, 8195–8211 (2021).

35. Saturno, J. et al. African volcanic emissions influencing atmospheric aerosols over the Amazon rain forest. *Atmos. Chem. Phys.* **18**, 10391–10405 (2018).

36. Moteki, N. et al. Size dependence of wet removal of black carbon aerosols during transport from the boundary layer to the free troposphere. *Geophys. Res. Lett.* **39**, 2–5 (2012).

37. Fierce, L., Riemer, N. & Bond, T. C. Explaining variance in black carbon's aging timescale. *Atmos. Chem. Phys.* **15**, 3173–3191 (2015).

38. Wu, H. et al. Rapid transformation of ambient absorbing aerosols from west African biomass burning. *Atmos. Chem. Phys.* **21**, 9417–9440 (2021).

39. Sedlacek, A. J. I. et al. Using the black carbon particle mixing state to characterize the lifecycle of biomass burning aerosols. *Environ. Sci. Technol.* **56**, 14315–14325 (2022).

40. Che, H. et al. Cloud processing and weeklong ageing affect biomass burning aerosol properties over the south-eastern Atlantic. *Commun. Earth Environ.* **3**, 182 (2022).

41. Martin, S. et al. The Green Ocean Amazon Experiment (GoAmazon2014/5) observes pollution affecting gases, aerosols, clouds, and rainfall over the rain forest. *Bulletin American Meteorol. Society.* **0**, 981–997 (2016).

42. Schwarz, J. P. et al. Measurement of the mixing state, mass, and optical size of individual black carbon particles in urban and biomass burning emissions. *Geophys. Res. Lett.* **35**, 1–5 (2008).

43. Andrés Hernández, M. D. et al. Overview: On the transport and transformation of pollutants in the outflow of major population centres – observational data from the EMeRGe European intensive operational period in summer 2017. *Atmos. Chem. Phys.* **22**, 5877–5924 (2022).

44. Saturno, J. et al. Black and brown carbon over central Amazonia: long-term aerosol measurements at the ATTO site. *Atmos. Chem. Phys.* **18**, 12817–12843 (2018).

45. Malecha, K. T. & Nizkorodov, S. A. Photodegradation of secondary organic aerosol particles as a source of small, oxygenated volatile organic compounds. *Environ. Sci. Technol.* **50**, 9990–9997 (2016).

46. Bond, T. C. et al. Bounding the role of black carbon in the climate system: A scientific assessment. *J. Geophys. Res. Atmos.* **118**, 5380–5552 (2013).

47. Denjean, C. et al. Overview of aerosol optical properties over southern west Africa from dacciwa aircraft measurements. *Atmos. Chem. Phys.* **20**, 4735–4756 (2020).

48. Bond, T. C. & Bergstrom, R. W. Light Absorption by Carbonaceous Particles: An Investigative Review. *Aerosol Sci. Technol.* **40**, 27–67 (2006).

49. Fierce, L., Bond, T. C., Bauer, S. E., Mena, F. & Riemer, N. Black carbon absorption at the global scale is affected by particle-scale diversity in composition. *Nat. Commun.* **7**, 1–8 (2016).

50. Andreae, M. O. & Gelencser, A. Black carbon or brown carbon? the nature of light-absorbing carbonaceous aerosols. *Atmos. Chem. Phys.* **6**, 3131–3148 (2006).

51. Saleh, R. et al. Absorptivity of brown carbon in fresh and photo-chemically aged biomass-burning emissions. *Atmos. Chem. Phys.* **13**, 7683–7693 (2013).

52. Corbin, J. C. et al. Brown and black carbon emitted by a marine engine operated on heavy fuel oil and distillate fuels: Optical properties, size distributions, and emission factors. *J. Geophys. Res. Atmos.* **123**, 6175–6195 (2018).

53. Schuster, G. L., Dubovik, O. & Holben, B. N. Angstrom exponent and bimodal aerosol size distributions. *J. Geophys. Res.* **111**, D07207 (2006).

54. Jöckel, P. et al. Earth system chemistry integrated modelling (escimo) with the modular earth submodel system (messy) version 2.51. *Geosci. Model Dev.* **9**, 1153–1200 (2016).

55. Danabasoglu, G. et al. The community earth system model version 2 (cesm2). *J. Adv. Modeling Earth Sys.* **12**, e2019MS001916 (2020).

56. Lund, M. T. et al. Short Black Carbon lifetime inferred from a global set of aircraft observations. *npj Climate Atmos. Sci.* **1**, 1–8 (2018).

57. Mallet, M. et al. Simulation of the transport, vertical distribution, optical properties and radiative impact of smoke aerosols with the aladin regional climate model during the ORACLES-2016 and LASIC experiments. *Atmos. Chem. Phys.* **19**, 4963–4990 (2019).

58. Shinozuka, Y. et al. Modeling the smoky troposphere of the southeast Atlantic: a comparison to ORACLES airborne observations from September of 2016. *Atmos. Chem. Phys.* **20**, 11491–11526 (2020).

59. Ramo, R. et al. African burned area and fire carbon emissions are strongly impacted by small fires undetected by coarse resolution satellite data. *Proc. Natl. Acad. Sci.* **118**. https://www.pnas.org/content/118/9/e2011160118.full.pdf (2021).

60. Bond, W. & Zaloumis, N. P. The deforestation story: testing for anthropogenic origins of Africa's flammable grassy biomes. *Philosophical Trans. Royal Society B: Biol. Sci.* **371**, 20150170 (2016).

61. Hamilton, D. S. et al. Earth, wind, fire, and pollution: Aerosol nutrient sources and impacts on ocean biogeochemistry. *Ann. Rev. Marine Sci.* **14**, 303–330 (2022).

62. Yáñez-Serrano, A. M. et al. Monoterpene chemical speciation in a tropical rainforest: variation with season, height, and time of day at the Amazon Tall Tower Observatory (ATTO). *Atmos. Chem. Phys.* **18**, 3403–3418 (2018).

63. Botía, S. et al. Understanding nighttime methane signals at the Amazon Tall Tower Observatory (ATTO). *Atmos. Chem. Phys.* **20**, 6583–6606 (2020).

64. Löbs, N. et al. Aerosol measurement methods to quantify spore emissions from fungi and cryptogamic covers in the Amazon. *Atmos. Meas. Tech.* **13**, 153–164 (2020).

65. von der Weiden, S. L., Drewnick, F. & Borrmann, S. Particle loss calculator – a new software tool for the assessment of the performance of aerosol inlet systems. *Atmos. Meas. Tech.* **2**, 479–494 (2009).

66. Stephens, M., Turner, N. & Sandberg, J. Particle identification by laser-induced incandescence in a solid-state laser cavity. *Applied optics* **42**, 3726–36 (2003).

67. Schwarz, J. P. et al. Single-particle measurements of midlatitude black carbon and light-scattering aerosols from the boundary layer to the lower stratosphere. *J. Geophys. Res. Atmos.* **111**, 1–15 (2006).

68. Laborde, M. et al. Black carbon physical properties and mixing state in the European megacity Paris. *Atmos. Chem. Phys.* **13**, 5831–5856 (2013).

69. Gysel, M., Laborde, M., Olfert, J. S., Subramanian, R. & Gréhn, A. J. Effective density of Aquadag and fullerene soot black carbon reference materials used for SP2 calibration. *Atmos. Measurement Tech.* **4**, 2851–2858 (2011).

70. Gysel-Beer, M. & Corbin, J. SP2 toolkit 4.115 (Igor7) (Version 4.115). https://doi.org/10.5281/zenodo.3575186/ (2019).

71. Pileci, R. E. et al. Comparison of co-located refractory black carbon (rBC) and elemental carbon (EC) mass concentration measurements during field campaigns at several European sites. *Atmos. Measurement Tech.* **14**, 1379–1403 (2021).

72. Gao, R. S. et al. A Novel Method for Estimating Light-Scattering Properties of Soot Aerosols Using a Modified Single-Particle Soot Photometer. *Aerosol Sci. Technol.* **41**, 125–135 (2007).

73. Yuan, J. et al. Variability in the mass absorption cross section of black carbon (BC) aerosols is driven by BC internal mixing state at a central European background site (Melpitz, Germany) in winter. *Atmos. Chem. Phys.* **21**, 635–655 (2021).

74. Motos, G. et al. Black Carbon Aerosols in the Lower Free Troposphere are Heavily Coated in Summer but Largely Uncoated in Winter at Jungfraujoch in the Swiss Alps. *Geophys. Res. Lett.* **47**, 1–10 (2020).

75. Pöhlker, M. L. et al. Long-term observations of cloud condensation nuclei in the Amazon rain forest – part 1: Aerosol size distribution, hygroscopicity, and new model parameterizations for CCN prediction. *Atmos. Chem. Phys.* **16**, 15709–15740 (2016).

76. Franco, M. A. et al. Occurrence and growth of sub-50 nm aerosol particles in the Amazonian boundary layer. *Atmos. Chem. Phys.* **22**, 3469–3492 (2022).

77. Machado, L. A. T. et al. How weather events modify aerosol particle size distributions in the Amazon boundary layer. *Atmos. Chem. Phys.* **21**, 18065–18086 (2021).

78. Ng, N. L. An aerosol chemical speciation monitor (acsm) for routine monitoring of the composition and mass concentrations of ambient aerosol. *Aerosol Sci. Technol.* **45**, 780–794 (2011).

79. Schulz, C. et al. Aircraft-based observations of isoprene epoxydiol-derived secondary organic aerosol (IEPOX-SOA) in the tropical upper troposphere over the Amazon region. *Atmos. Chem. Phys. Discussions* 1–32. https://www.atmos-chem-phys-discuss.net/acp-2018-232/ (2018).

80. de Sá, S. S. et al. Urban influence on the concentration and composition of submicron particulate matter in central Amazonia. *Atmos. Chem. Phys.* **18**, 12185–12206 (2018).

81. de Sá, S. S. et al. Contributions of biomass-burning, urban, and biogenic emissions to the concentrations and light-absorbing properties of particulate matter in central Amazonia during the dry season. *Atmos. Chem. Phys.* **19**, 7973–8001 (2019).

82. Wu, H. et al. Vertical variability of the properties of highly aged biomass burning aerosol transported over the southeast Atlantic during CLARIFY-2017. *Atmos. Chem. Phys.* **20**, 12697–12719 (2020).

83. Taylor, J. W. et al. Absorption closure in highly aged biomass burning smoke. *Atmos. Chem. Phys.* **20**, 11201–11221 (2020).
84. Collaud Coen, M. et al. Minimizing light absorption measurement artifacts of the aethalometer: evaluation of five correction algorithms. *Atmos. Meas. Tech.* **3**, 457–474 (2010).
85. Saturno, J. et al. Comparison of different aethalometer correction schemes and a reference multi-wavelength absorption technique for ambient aerosol data. *Atmos. Meas. Tech.* **10**, 2837–2850 (2017).
86. Andreae, M. O. et al. Aerosol characteristics and particle production in the upper troposphere over the Amazon Basin. *Atmos. Chem. Phys.* **18**, 921–961 (2018).
87. Schneider, J. et al. Aircraft-based observation of meteoric material in lower-stratospheric aerosol particles between 15 and 68° N. *Atmos. Chem. Phys.* **21**, 989–1013 (2021).
88. Baars, H. et al. Aerosol profiling with lidar in the Amazon Basin during the wet and dry season. *J. Geophys. Res. Atmos.* **117**, 1–16 (2012).
89. Heintzenberg, J. Properties of the log-normal particle size distribution. *Aerosol Sci. Technol.* **21**, 46–48 (1994).
90. Draxler, R. R. & Hess, G. D. An overview of the hysplit_4 modelling system for trajectories, dispersion and deposition. *Australian Meteorol. Magazine.* **47**, 295–308 (1998).
91. Stein, A. F. et al. NOAA's HYSPLIT atmospheric transport and dispersion modeling system. *Bulletin American Meteor. Society.* **96**, 2059–2077 (2015).
92. Jöckel, P., Sander, R., Kerkweg, A., Tost, H. & Lelieveld, J. Technical Note: The Modular Earth Submodel System (MESSy) - a new approach towards Earth System Modeling. *Atmos. Chem. Phys.* **5**, 433–444 (2005).
93. Jöckel, P. et al. Development cycle 2 of the Modular Earth Submodel System (MESSy2). *Geosci. Model Dev.* **3**, 717–752 (2010).
94. Pozzer, A. et al. Distributions and regional budgets of aerosols and their precursors simulated with the EMAC chemistry-climate model. *Atmos. Chem. Phys.* **12**, 961–987 (2012).
95. Lelieveld, J. et al. Cardiovascular disease burden from ambient air pollution in Europe reassessed using novel hazard ratio functions. *Eur Heart J* **40**, 1590–1596 (2019).
96. Beer, C. G. et al. Modelling mineral dust emissions and atmospheric dispersion with MADE3 in EMAC v2.54. *Geosci. Model Dev.* **13**, 4287–4303 (2020).
97. Pringle, K. J. et al. Description and evaluation of GMXe: a new aerosol submodel for global simulations (v1). *Geosci. Model Dev.* **3**, 391–412 (2010).
98. Paasonen, P. et al. Continental anthropogenic primary particle number emissions. *Atmos. Chem. Phys.* **16**, 6823–6840 (2016).
99. Tsimpidi, A. P., Karydis, V. A., Pozzer, A., Pandis, S. N. & Lelieveld, J. ORACLE (v1.0): module to simulate the organic aerosol composition and evolution in the atmosphere. *Geosci. Model Dev.* **7**, 3153–3172 (2014).
100. Tsimpidi, A. P., Karydis, V. A., Pozzer, A., Pandis, S. N. & Lelieveld, J. ORACLE 2-D (v2.0): an efficient module to compute the volatility and oxygen content of organic aerosol with a global chemistry–climate model. *Geosci. Model Dev.* **11**, 3369–3389 (2018).
101. Lauer, A., Eyring, V., Hendricks, J., Jöckel, P. & Lohmann, U. Global model simulations of the impact of ocean-going ships on aerosols, clouds, and the radiation budget. *Atmos. Chem. Phys.* **7**, 5061–5079 (2007).
102. Dietmüller, S. et al. A new radiation infrastructure for the Modular Earth Submodel System (MESSy, based on version 2.51). *Geosci. Model. Dev.* **9**, 2209–2222 (2016).
103. Klingmüller, K., Lelieveld, J., Karydis, V. A. & Stenchikov, G. L. Direct radiative effect of dust–pollution interactions. *Atmos. Chem. Phys.* **19**, 7397–7408 (2019).
104. Sander, R., Kerkweg, A., Jöckel, P. & Lelieveld, J. Technical note: The new comprehensive atmospheric chemistry module MECCA. *Atmos. Chem. Phys.* **5**, 445–450 (2005).
105. Sander, R. et al. The community atmospheric chemistry box model CAABA/MECCA-4.0. *Geosci. Model Dev.* **12**, 1365–1385 (2019).
106. Lelieveld, J. et al. Stratospheric dryness: model simulations and satellite observations. *Atmos. Chem. Phys.* **7**, 1313–1332 (2007).
107. Kerkweg, A., Sander, R., Tost, H. & Jöckel, P. Technical note: Implementation of prescribed (OFFLEM), calculated (ONLEM), and pseudo-emissions (TNUDGE) of chemical species in the Modular Earth Submodel System (MESSy). *Atmos. Chem. Phys.* **6**, 3603–3609 (2006).
108. Lelieveld, J. et al. Effects of fossil fuel and total anthropogenic emission removal on public health and climate. *Proc. Natl. Acad. Sci.* **116**, 7192–7197 (2019).
109. Brühl, C., Lelieveld, J., Tost, H., Höpfner, M. & Glatthor, N. Stratospheric sulfur and its implications for radiative forcing simulated by the chemistry climate model EMAC. *J. Geophys. Res. Atmos.* **120**, 2103–2118 (2015).
110. Pozzer, A. et al. AOD trends during 2001–2010 from observations and model simulations. *Atmos. Chem. Phys.* **15**, 5521–5535 (2015).
111. Zimmermann, P. H. et al. Model simulations of atmospheric methane (1997–2016) and their evaluation using NOAA and AGAGE surface and IAGOS-CARIBIC aircraft observations. *Atmos. Chem. Phys.* **20**, 5787–5809 (2020).
112. Chowdhury, S. et al. Global and national assessment of the incidence of asthma in children and adolescents from major sources of ambient NO2. *Environ. Res. Lett.* **16**, 035020 (2021).
113. Hoesly, R. M. et al. Historical (1750–2014) anthropogenic emissions of reactive gases and aerosols from the community emissions data system (ceds). *Geosci. Model Dev.* **11**, 369–408 (2018).
114. Kaiser, J. W. et al. Biomass burning emissions estimated with a global fire assimilation system based on observed fire radiative power. *Biogeosciences* **9**, 527–554 (2012).
115. Pan, X. et al. Six global biomass burning emission datasets: intercomparison and application in one global aerosol model. *Atmos. Chem. Phys.* **20**, 969–994 (2020).
116. Reifenberg, S. F. et al. Numerical simulation of the impact of COVID-19 lockdown on tropospheric composition and aerosol radiative forcing in Europe. *Atmosph. Chem. Phys.* **22**, 10901–10917 (2022).
117. Pozzer, A. et al. Simulation of organics in the atmosphere: evaluation of EMACv2.54 with the Mainz Organic Mechanism (MOM) coupled to the ORACLE (v1.0) submodel. *Geosci. Model Dev.* **15**, 2673–2710 (2022).
118. Krüger, O. O. et al. Black carbon aerosol reductions during COVID-19 confinement quantified by aircraft measurements over Europe. *Atmos. Chem. Phys.* **22**, 8683–8699 (2022).
119. Lin, S.-J. & Rood, R. B. An explicit flux-form semi-lagrangian shallow-water model on the sphere. *Quarterly J. Royal Meteorol. Society.* **123**, 2477–2498 (1997).
120. Emmons, L. K. et al. The chemistry mechanism in the community earth system model version 2 (CESM2). *J. Adv. Modeling Earth Sys.* **12**, e2019MS001882 (2020).
121. Liu, X. et al. Description and evaluation of a new four-mode version of the modal aerosol module (MAM4) within version 5.3 of the community atmosphere model. *Geosci. Model Dev.* **9**, 505–522 (2016).
122. Hurrell, J. W., Hack, J. J., Shea, D., Caron, J. M. & Rosinski, J. A new sea surface temperature and sea ice boundary dataset for the community atmosphere model. *J. Climate.* **21**, 5145 – 5153 (2008).
123. Darmenov, A. S. & da Silva, A. The Quick Fire Emissions Dataset (QFED)–Documentation of versions 2.1, 2.2 and 2.4. *NASA//TM-2015-104606* **38**, 183 pp (2015).
124. Gelaro, R. et al. The Modern-Era Retrospective Analysis for Research and Applications, Version 2 (MERRA-2). *J. Climate.* **30**, 5419–5454 (2017).
125. Chin, M. et al. Tropospheric Aerosol Optical Thickness from the GOCART Model and Comparisons with Satellite and Sun Photometer Measurements. *J. Atmosph. Sci.* **59**, 461–483 (2002).
126. Colarco, P., da Silva, A., Chin, M. & Diehl, T. Online simulations of global aerosol distributions in the NASA GEOS-4 model and comparisons to satellite and ground-based aerosol optical depth. *J. Geophys. Res.* **115**, D14207 (2010).
127. Rienecker, M. et al. The GEOS-5 Data Assimilation System–Documentation of versions 5.0.1, 5.1.0, and 5.2.0. *NASA/TM–2008–104606* **27**, 118 (2008).
128. Randles, C. A. The MERRA-2 Aerosol Assimilation. *NASA Tech. Report.* **45**, 1–140 (2016).
129. Randles, C. A. et al. The MERRA-2 Aerosol Reanalysis, 1980 Onward. Part I: System Description and Data Assimilation Evaluation. *J. Climate.* **30**, 6823–6850 (2017).
130. Buchard, V. et al. The MERRA-2 Aerosol Reanalysis, 1980 Onward. Part II: Evaluation and Case Studies. *J. Climate.* **30**, 6851–6872 (2017).
131. Reichle, R. H. et al. Land Surface Precipitation in MERRA-2. *J. Climate.* **30**, 1643–1664 (2017).
132. Nowottnick, E. et al. Online simulations of mineral dust aerosol distributions: Comparisons to NAMMA observations and sensitivity to dust emission parameterization. *J. Geophys. Res.* **115**, D03202 (2010).
133. Nowottnick, E., Colarco, P., da Silva, A., Hlavka, D. & McGill, M. The fate of Saharan dust across the Atlantic and implications for a central American dust barrier. *Atmosph. Chem. Phys.* **11**, 8415–8431 (2011).
134. Bian, H. et al. Source attributions of pollution to the Western Arctic during the NASA ARCTAS field campaign. *Atmosph. Chem. Phys.* **13**, 4707–4721 (2013).
135. Holanda, B. & Pöhlker, C. Data on influx of African smoke into the Amazon. https://doi.org/10.17617/3.YTLQYH (2023).

Acknowledgements

Author contributions

Funding

Competing interests

The authors declare no competing interest.

Additional information

Supplementary information The online version contains supplementary material available at https://doi.org/10.1038/s43247-023-00795-5.

Correspondence and requests for materials should be addressed to Christopher Pöhlker.

Peer review information *Communications Earth & Environment* thanks the anonymous reviewers for their contribution to the peer review of this work. Primary Handling Editor: Aliénor Lavergne. Peer reviewer reports are available.

Reprints and permission information is available at http://www.nature.com/reprints

Publisher's note Springer Nature remains neutral with regard to jurisdictional claims in published maps and institutional affiliations.